ARTICLE

Cascaded energy landscape as a key driver for slow yet efficient charge separation with small energy offset in organic solar cells

Received 00th January 20xx,
Accepted 00th January 20xx

DOI: 10.1039/x0xx00000x

Shin-ichiro Natsuda,[a] Toshiharu Saito,[a] Rei Shirouchi,[a] Yuji Sakamoto,[a] Taiki Takeyama,[a] Yasunari Tamai*[a,b], Hideo Ohkita[a]

Recent studies have shown that efficient free carrier (FC) generation with a small voltage loss can be achieved in organic solar cells (OSCs); however, the photophysical insights underpinning this remain unclear. Herein, we examined the mechanisms underlying the FC generation in a state-of-the-art OSC consisting of PM6 and Y6 as electron donor and acceptor, respectively, wherein the energy offset between the lowest excited singlet state and the charge transfer state is as small as ~0.12 eV. We used transient absorption spectroscopy to track the time evolution of electroabsorption caused by electron–hole pairs generated at donor/acceptor interfaces. After hole transfer from Y6 to PM6, we observed slow yet efficient spatial charge dissociation on a time scale of picoseconds. Based on temperature-dependence measurements, we found that this slow yet efficient FC generation is driven by downhill energy relaxation of charges through the energy cascade generated near the interfaces. We provide here direct experimental evidence for the FC generation mechanism in the very topical PM6/Y6 blend system.

Introduction

Development of novel nonfullerene acceptors (NFAs) has enabled the successful fabrication of efficient polymer/NFA-based organic solar cells (OSCs).[1–5] Thus far, polymer/NFA-based OSCs have reached >18% power conversion efficiency (PCE),[6–9] thereby rekindling interest in this research field. Among them, a state-of-the-art OSC consisting of PM6 as a donor polymer and Y6 as a NFA (Figs. 1d and 1e) has simultaneously exhibited a relatively high PCE of >15% and a small energy loss of ~0.55 eV.[10] In this respect, many studies have been conducted in order to reveal the origin of the success of the PM6/Y6 blend OSCs.[11–19] However, the photophysical mechanisms underlying efficient free carrier (FC) generation in this blend system remain the subject of continuing debate.

OSCs require a donor/acceptor (D/A) interface to dissociate excitons into charges because of the low dielectric constants of organic materials. Upon photoexcitation, singlet excitons are generated in either the D or A material and quickly diffuse to the D/A interface. Thereafter, depending on which material is photoexcited, either an electron or a hole is transferred to its counterpart material, forming a charge transfer (CT) state at the D/A interface. If the electrons and holes that constitute the CT state dissociate beyond their Coulomb capture radius (typically 4–5 nm considering the entropic contribution to the Gibbs free energy),[20] they become FCs and can survive up to microseconds, which is long enough for charges to be collected to their respective electrodes. Historically, it was presumed that a large offset between the lowest excited singlet state energy E_{S1} and the CT state energy E_{CT} of >0.3 eV is required for efficient FC generation in OSCs.[20–24] For example, Friend and his co-workers have elucidated that this excess energy is required to access higher-energy delocalized states, wherein charges can move quickly away from the D/A interface on a time scale of tens to a few hundreds of femtoseconds.[25–29] On the other hand, in the absence of the offset energy (or the absence of a delocalized state in less-aggregated blends), the CT state is trapped at the interface and finally undergoes geminate recombination to the ground state. The large energy offset prerequisite for efficient FC generation significantly limits the PCE because lowering E_{CT} relative to E_{S1} reduces the maximum achievable open-circuit voltage (V_{OC}).[30–33] Therefore, efficient FC generation without an energy offset is necessary to reduce the voltage loss, and hence, improve the PCE further.

Very few studies have reported polymer/fullerene-based OSCs that exhibit efficient FC generation with small energy offset.[34–36] In contrast, recent studies have shown that efficient FC generation with small energy offset can be achieved in various NFA-based OSCs. Several key ideas have been proposed for the FC generation mechanisms in systems with small energy offset. For example, Menke et al. proposed that a low level of energetic disorder, which corresponds to an Urbach energy of <30 meV, is key to efficient FC generation in small offset systems.[37] The PM6/Y6 blends fulfil this empirical requirement. On the other hand, Karuthedath et al. claimed that the ionization energy (IE) offsets are often underestimated in OSCs.[38] By performing ultraviolet photoelectron spectroscopy (UPS) measurements, they showed that the IE offset in the PM6/Y6 blend was as large as 700 meV and proposed that a large IE offset of >500 meV is required to attain an internal quantum

[a] Department of Polymer Chemistry, Graduate School of Engineering, Kyoto University, Katsura, Nishikyo, Kyoto 615-8510, Japan
[b] Japan Science and Technology Agency (JST), PRESTO, 4-1-8 Honcho Kawaguchi, Saitama 332-0012, Japan

Electronic Supplementary Information (ESI) available: [details of any supplementary information available should be included here]. See DOI: 10.1039/x0xx00000x

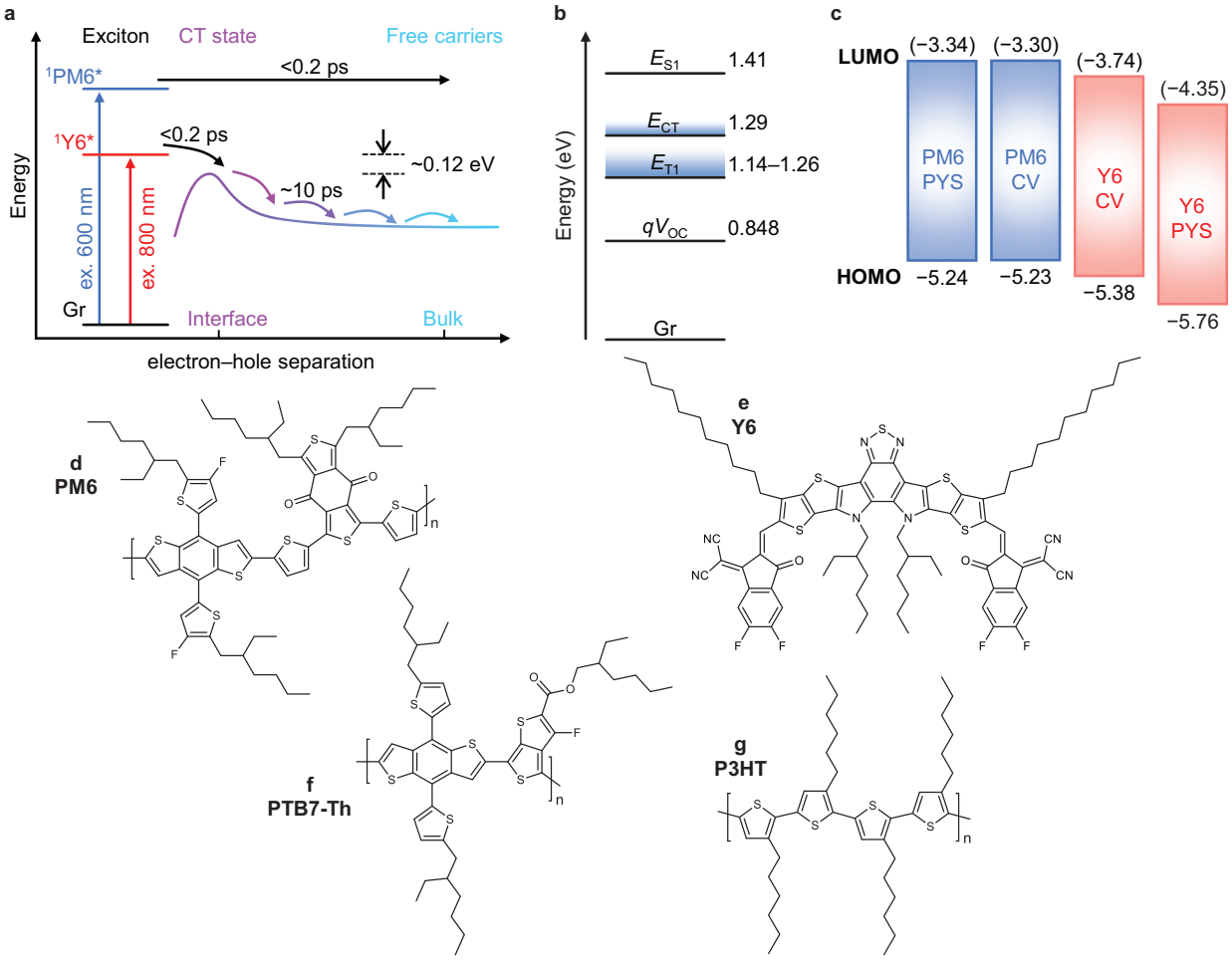

Fig. 1. **a** Schematic showing FC generation mechanisms in the PM6/Y6 blend films. Upon photoexcitation at 800 nm, spatial dissociation of electron–hole pairs occurs slowly yet efficiently without an activation barrier, despite the small energy offset of ~0.12 eV, driven by downhill energy relaxation of charges through the energy cascade near the interfaces. In contrast, rapid spatial separation on a sub-picosecond time scale occurs after photoexcitation at 600 nm. **b** Energy levels of relevant states. E_{CT} contains some uncertainty. E_{T1} is taken from our previous study.[39] **c** HOMO energy levels of PM6 and Y6 determined by CV or PYS. The values in parentheses are the LUMO energy levels calculated as a sum of HOMO and E_{S1}. Therefore, the LUMO values only serve as a rough estimate for relative comparison. **d-g** Chemical structures of materials employed in this study.

efficiency of >80% because of the interfacial energy level bending caused by electrostatic effects, which in turn are caused by the large quadrupole moments of A–D–A-type NFAs. However, due to the lack of direct experimental evidence, the FC generation mechanism has only been speculated or reported on the basis of indirect evidence; hence, further studies are required to fully understand the FC generation mechanisms in the PM6/Y6 blend system.

Herein, we examine the FC generation mechanisms in the PM6/Y6 blend system using transient absorption (TA) spectroscopy. We track the time evolution of electroabsorption (EA) caused by the dipolar electric field generated by an electron–hole pair that constitutes a CT state. We show that, after hole transfer from Y6 to PM6, FCs are generated slowly yet efficiently on a time scale of ~10 ps. This is in sharp contrast to the FC generation dynamics after photoexcitation of PM6, wherein rapid spatial separation is observed, as in the case of previously reported large offset systems. Importantly, despite the slow time scale, FC generation after the hole transfer is as efficient as that after the electron transfer and no thermal activation barriers exist for the FC generation. We find that charge dissociation is driven by downhill energy relaxation of charges through the energy cascade generated near the D/A interface (Fig. 1a).

Results and discussions

Energy offset in the PM6/Y6 blend systems

Chemical structures of materials employed in this study, steady-state absorption, photoluminescence (PL) and electroluminescence (EL) spectra, the highest occupied molecular orbital (HOMO) energy levels, current density–voltage (*J–V*) characteristics, and external quantum efficiency (EQE) spectra are found in Figs. 1, 2 and in the Supplementary Information, Figs. S1–S11. The absorption and PL spectra of Y6 slightly blueshift when blended with PM6, indicating that Y6 is slightly less ordered in the blend film than in the pristine Y6

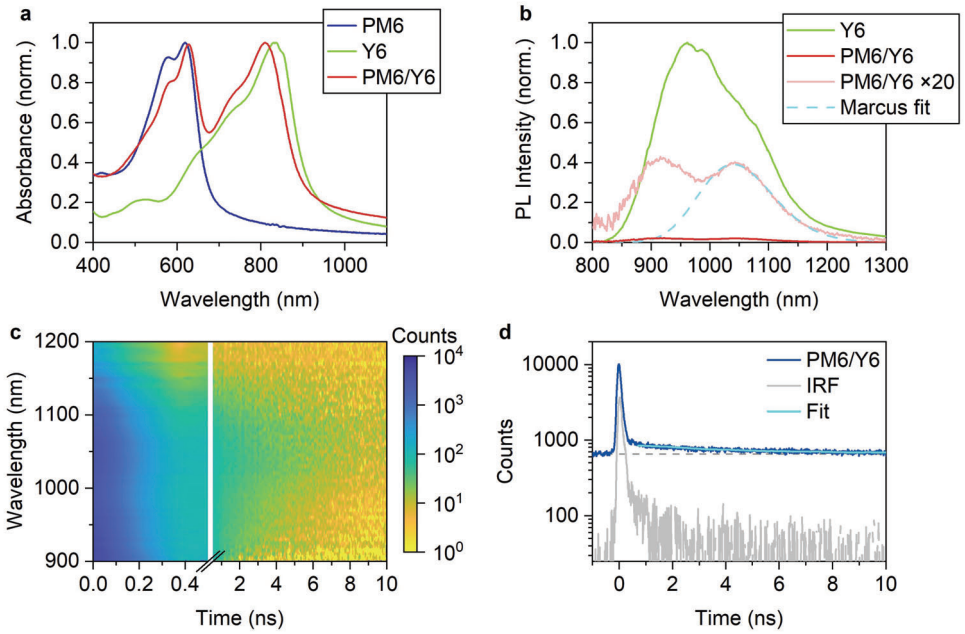

Fig. 2. **a** Steady-state absorption spectrum of an optimized PM6/Y6 blend film as well as pristine PM6 and Y6 films. **b** PL spectrum of the PM6/Y6 blend film as well as a pristine Y6 film. The broken line represents emission from the CT states obtained by the Marcus fitting. **c** TRPL spectra of the PM6/Y6 blend film. **d** PL decay monitored at 1050 nm. The full width at half maximum (fwhm) of the instrument response function (IRF) is 160 ps. The broken horizontal line in (**d**) is the base line as a guide for the eye. The decay time constant was determined by analyzing the slower decay component.

film (Fig. 2a). In the blend film, E_{S1} of Y6 is 1.41 eV (Fig. S2), which is slightly higher than that of the pristine Y6 film (1.39 eV).[39] As shown in Fig. 2b, a new PL band peaking at ~1050 nm appears for the PM6/Y6 blend. This band is not observed for the PTB7-Th/Y6 blend (Fig. S6), indicating that it is attributable to CT emission of the PM6/Y6 blend. We confirmed this by measuring the time-resolved PL (TRPL) spectra of the PM6/Y6 blend, as shown in Fig. 2c. The PM6/Y6 blend clearly exhibits a longer decay component peaking at ~1050 nm (the PL spectra at each time can be found in Fig. S7). The longer decay component has the decay time constant of ~2.6 ns (Fig. 2d), which is much longer than the PL lifetime of pristine Y6 (~1.2 ns),[39] indicating that the attribution of the new PL band peaking at ~1050 nm to the CT emission is appropriate. By applying the Marcus fitting to the CT emission,[40,41] we obtained E_{CT} of 1.29 eV (details can be found in the Supplementary Information, Figs. S6 and S7). Therefore, the PM6/Y6 system apparently has a small energy offset of ~0.12 eV between E_{S1} and E_{CT}. Note that the last digit of this energy offset carries some degree of error owing to the uncertainty in E_{CT}, as mentioned in the Supplementary Information. Energy levels are summarized in Fig. 1b.

We measured the difference in HOMO energy between PM6 and Y6 using two different methods, as summarized in Fig. 1c. The HOMO energy offset derived from cyclic voltammetry (CV) in the solution state was 0.15 eV (Fig. S8), consistent with the energy offset between E_{S1} and E_{CT}. In contrast, the IE offset derived from photoelectron yield spectroscopy (PYS) in the solid state was as large as 0.52 eV (Fig. S9), which is significantly larger than that derived from CV measurements in the solution state. These results indicate that the HOMO energy level, and hence, the lowest unoccupied molecular orbital (LUMO) energy level, of Y6 depends significantly on its morphology. In other words, Y6 in crystalline states has a deeper HOMO and LUMO energy levels than that in amorphous states. We consider that the large difference in the HOMO and LUMO energy levels of Y6 depending on the morphology is key for efficient FC generation with a small offset, as will be discussed later. We believe that the HOMO energy levels obtained from CV in the solution state represent the nature of the real D/A interface more accurately than that from PYS in the solid state because materials are less ordered at D/A interfaces. This is consistent with the relatively small V_{OC} loss of this system, which is discussed in more detail later (*vide infra*).

TA spectra after Y6 selective excitation

In order to study the charge dissociation dynamics, we performed TA measurements for the optimized PM6/Y6 blend film (Figs. 3a and 3b, summary of assignments of the TA spectra can be found in Fig. S12). Here, the excitation wavelength was set to 800 nm to selectively excite the lower-bandgap Y6. The excitation fluence was kept as low as possible to reduce undesirable bimolecular processes. At an excitation fluence of 1.4 μJ cm^{-2}, singlet–singlet annihilation (SSA) can be ignored (excitation-fluence dependence is shown in Fig. S19). By comparing the TA spectra of the blend with those of a pristine Y6 film (Fig. S13), the positive photoinduced absorption (PIA) band observed immediately after photoexcitation at ~930 nm and the broad PIA tail above 1200 nm are assigned to singlet excitons of Y6.[18,39,42] Negative signals in the 750–850 nm region and sub-650 nm regions are attributable to the ground-state bleaching (GSB) of Y6 and PM6, respectively, because the positions of these signals coincide with their steady-state absorption spectra. The initial peak position of the Y6 GSB is slightly blueshifted compared to that of the pristine Y6 film (Fig. 3c), which is consistent with the aforementioned slightly blueshifted steady-state absorption. Singlet excitons of Y6 decayed on a time scale of picoseconds, whereas a new PIA peaking

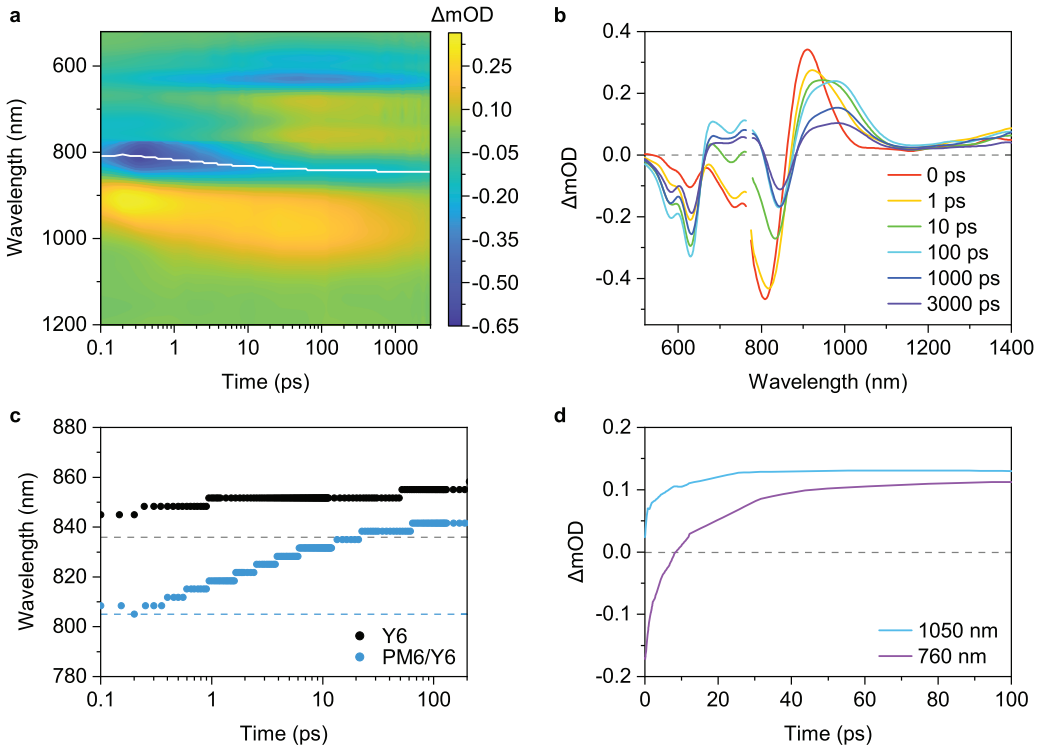

Fig. 3. **a** Contour plot of the TA data and **b** TA spectra of the optimized PM6/Y6 blend film. The excitation wavelength was 800 nm with a fluence of 1.4 μJ cm^{-2}. The white line in (**a**) represents the peak positions of Y6 GSB at each pump–probe delay. **c** Shift in the peak wavelength of Y6 GSB in the PM6/Y6 blend film (blue) as well as that in a pristine Y6 film (black) as a reference. The broken lines show the peak wavelength of respective steady-state absorption spectra. **d** Time evolution of TA signals monitored at 1050 nm (blue) and 760 nm (purple).

at ~970 nm remained over nanoseconds after photoexcitation. As described in detail in the Supplementary Information (Figs. S14–S16), this broad PIA can be assigned to the superposition of PM6 hole polarons and Y6 anions. This means that charges are generated through hole transfer from Y6 to PM6. The blue line in Fig. 3d represents the charge generation kinetics monitored at 1050 nm (low energy tail of charge PIA). The rise kinetics was fitted using the sum of two exponential functions with a constant fraction, giving an average rise time constant of ~6.0 ps. Note that the rise kinetics monitored at 630 nm (GSB of PM6) is identical to that at 1050 nm (Fig. S20). Emphatically, this relatively slow exciton dissociation does not directly mean that hole transfer is slow at the D/A interface because this rise kinetics is a convolution of exciton diffusion to D/A interfaces and hole transfer between Y6 and PM6.[43,44] To distinguish the rate-limiting process, we focused on the TA spectra in the visible region. Importantly, the GSB signal of PM6 in the <650 nm region was observed immediately after photoexcitation, indicating that Y6 excitons generated near the D/A interface undergo hole transfer within the time resolution of our TA setup (fwhm: ~140 fs). Furthermore, the rise time constant decreased with decreasing domain size of Y6 (Fig. S20). Therefore, the rise time constant of ~6.0 ps is governed by exciton diffusion to the D/A interfaces, and hole transfer between Y6 and PM6 occurs on the sub-picosecond time scale, despite the small energy offset. Hole transfer between Y6 and PM6 on the sub-picosecond time scale has also been reported previously.[18] This is in sharp contrast to recent observations, wherein hole transfer is considerably slow when D/A blends loose energy offset.[33,45-48] For example, Zhou et al., found that the hole transfer slows down monotonically by about two orders of magnitude from the sub-picosecond to several tenth of picoseconds when the energy offset decreases from ~0.5 eV to ~0 eV.[48] Note that the slow hole transfer does not directly lead a low hole transfer quantum yield because it is determined by the competition with the intrinsic exciton decay rate.[45,48] Fast hole transfer in the PM6/Y6 blend was also observed after photoexcitation at 900 nm (1.38 eV), where excess photon energy above E_{S1} is negligible (Fig. S21). Therefore, the possibility of rapid hole transfer from vibronically hot Y6 excitons can be ruled out. According to Marcus theory,[49] fast hole transfer with a small offset is expected to require a large D–A electronic coupling and/or a small reorganization energy. Density functional theory (DFT) calculations revealed that the reorganization energy during the hole transfer is ~0.27 eV (see the Supplementary Information, Figs. S22 and S23), which is considerably larger than the energy offset of this blend (~0.12 eV). Therefore, we speculate that a large D–A electronic coupling may be key for the fast hole transfer. The possibility of the large D–A electronic coupling has been also pointed out in a previous study, wherein the authors pointed out that the PM6 side chains and Y6 aromatic groups are in close contact in the active layer as observed using solid-state NMR measurements.[18] As we focus on the spatial dissociation of CT states into FCs in this study, revealing the exact origin of the fast hole transfer is beyond the scope of this study. A currently ongoing study highlights the fast hole transfer.

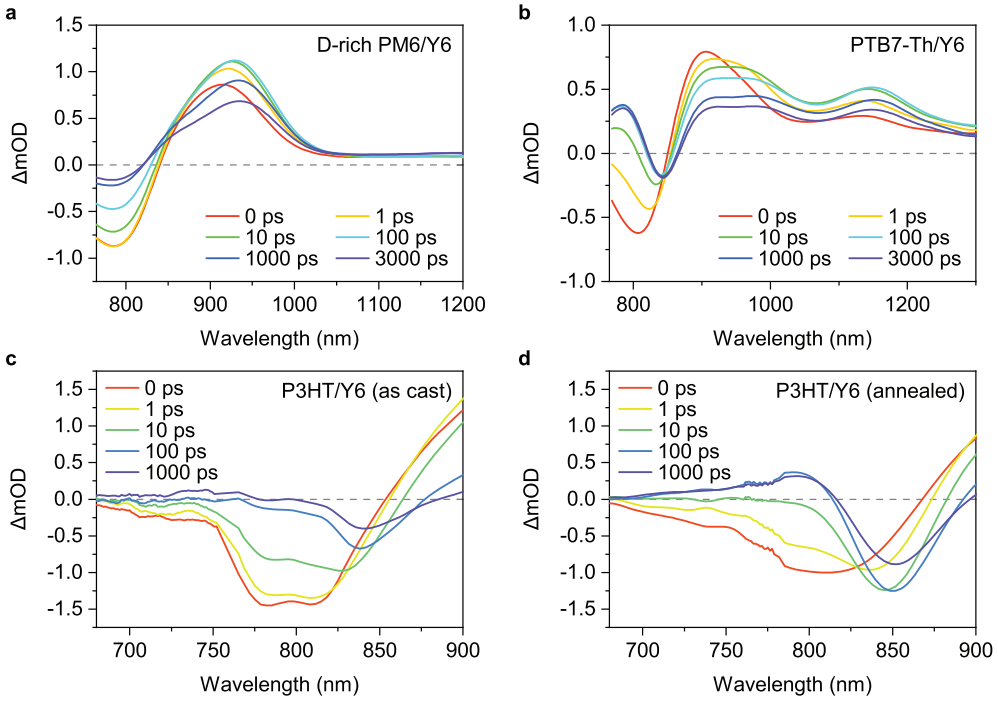

Fig. 4. **a** TA spectra of a D-rich PM6/Y6 blend film (95:5 w/w). The excitation wavelength was 800 nm with a fluence of 3.2 μJ cm^{-2}. **b** TA spectra of a PTB7-Th/Y6 blend film. The excitation wavelength was 800 nm with a fluence of 2.4 μJ cm^{-2}. **c,d** TA spectra of a P3HT/Y6 blend film measured (**c**) before and (**d**) after thermal annealing at 140 °C for 10 min. Full-range TA data can be found in the Supplementary Information, Fig. S17.

Interestingly, in the 700–800 nm region of Figs. 3a and 3b, the TA spectra changed significantly with time. Immediately after photoexcitation, we observed a negative TA signal attributable to Y6 GSB. Subsequently, this signal recovered rapidly and turned into a positive one over a >10 ps time scale. We identified two key features in this region. First, the rise time constant monitored at 760 nm was ~10.7 ps, which is slightly slower than that of exciton dissociation (Figs. 3d and S24). In other words, a time lag exists between the exciton dissociation and the emergence of a positive PIA at ~800 nm. Second, the peak position of Y6 GSB gradually redshifted with time (Figs. 3a and 3c). At 0 ps after photoexcitation, the peak wavelength of Y6 GSB was identical to that of the steady-state absorption (~810 nm), whereas it finally approached ~850 nm. This final peak position is approximately equal to that of the pristine Y6 film, indicating the presence of highly ordered crystalline Y6 domains in the blend film, even though the overall crystallinity is slightly lower than that of the pristine Y6 film, as mentioned above. This is consistent with the previously reported observation of a distinct π-π diffraction peak even in the blend film.[14] It should be noted that, while one might conclude that the Y6 GSB redshift is caused by an increase/decrease in the positive signals because the positive and negative TA signals overlap in a complex manner in this region, this scenario can safely be ruled out. For example, if the loss of the sharp Y6 singlet PIA, which overlaps with the low energy edge of the Y6 GSB, as a result of hole transfer could lead to a redshift, the peak position of the Y6 GSB in the PM6/Y6 blend film should be observed at a longer wavelength than that of the pristine Y6 film due to a mitigation of the overlap; however, the opposite is true, as shown in Fig. 3c. This scenario is also inconsistent with the fact that the Y6 GSB peak shifts more slowly than exciton dissociation (*vide infra*). Also, for the reason given above, the peak shift cannot be rationalized by an increase in the positive PIA at ~800 nm, which overlaps with the high energy edge of the Y6 GSB; i.e., the peak position of the Y6 GSB in the PM6/Y6 blend film should be observed at a longer wavelength than that of the pristine Y6 film due to the absence of the ~800 nm band in the pristine Y6 film (Fig. S13); however, the opposite is true. Therefore, we conclude that the redshift of the Y6 GSB peak in the blend film is an intrinsic characteristic of the Y6-based blend. The shift in the TA spectra is often observed for organic semiconductors in the solid state because their density of states is widely distributed in energy. As the GSB signal reflects the morphology in which the transient species resides at each time, the redshift of the GSB peak can be attributable to downhill energy relaxation of charges (see the Supplementary Information for more details), which is a key driver for FC generation in this blend, as will be further discussed later.

Impact of Y6 crystallinity on the TA spectra

In order to reveal the origin of the new PIA band in the 700–800 nm region, we also performed TA measurements on a D-rich PM6/Y6 blend film with a weight ratio of 95:5. As shown in Fig. S4, the peak position of the steady-state absorption spectrum of Y6 in the D-rich blend is somewhat blueshifted relative to that of the optimized PM6/Y6 blend film, indicating that Y6 is less aggregated in the D-rich blend film. Fig. 4a shows the TA spectra of the D-rich PM6/Y6 blend film after the selective excitation of Y6 at 800 nm. Interestingly, the D-rich blend did not exhibit a positive signal around 800 nm and the shift in the GSB peak, which strongly suggests that both the formation of the new PIA band and the shift in the GSB peak are driven by the presence of highly ordered regions in Y6 domains.

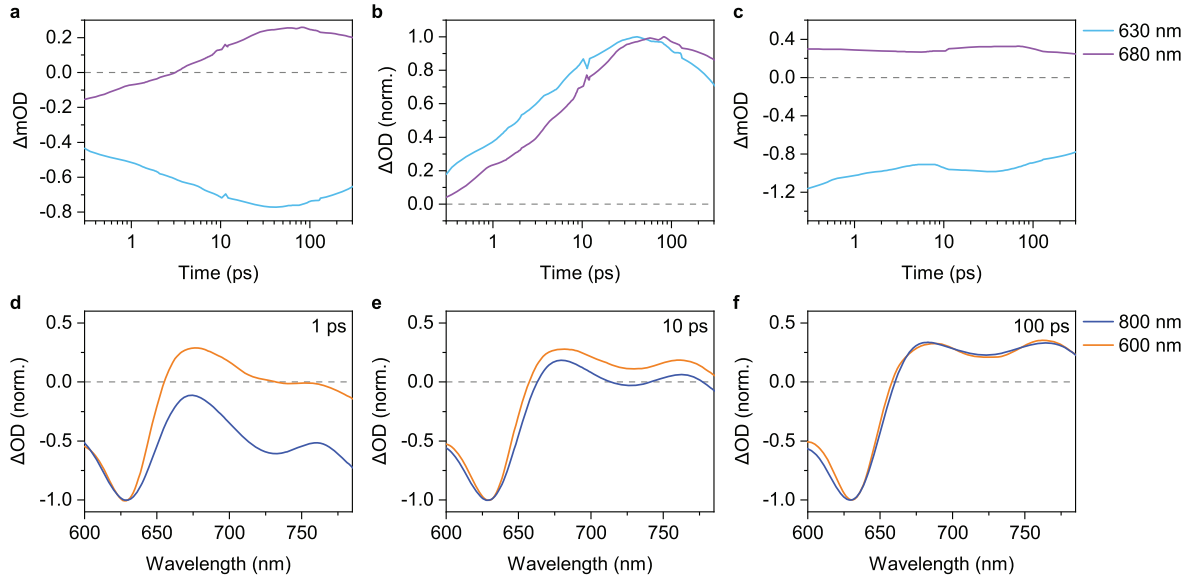

Fig. 5. **a** Time evolution of the TA signals monitored at 630 nm (PM6 GSB) and 680 nm (PM6 EA) excited at 800 nm. **b** Normalized time evolution of (**a**). Details of the normalization procedures are found in the Supplementary Information. **c** Time evolution of the TA signals monitored at 630 nm (PM6 GSB) and 680 nm (PM6 EA) excited at 600 nm. **d-f** Comparison of the TA spectra after photoexcitation at 800 nm or 600 nm with a pump–probe delay of (**d**) 1 ps, (**e**) 10 ps, and (**f**) 100 ps. TA spectra are normalized at 630 nm (PM6 GSB).

To obtain more detailed insights, we performed TA measurements on various D/A blend films (Figs. 4b-d). In the PTB7-Th/Y6 blend, dissociation of Y6 excitons occurs with a time constant of ~2.0 ps (Figs. 4b and S16b), whereas the emergence of the positive PIA was as slow as ~11.5 ps (Fig. S16c). These results strongly substantiate our hypothesis that the emergence of the positive PIA in the 700–800 nm region is not accompanied by exciton dissociation. Since the acceptor material is the same but the donor is different in the PM6/Y6 and PTB7-Th/Y6 blend films, we attribute the new PIA observed near 800 nm to the Y6 anion in crystalline domains. Further details of the assignments of the TA spectra can be found in the Supplementary Information, Figs. S14–S18. Interestingly, the TA spectra of the P3HT/Y6 blend film showed a clear dependence on the crystallinity of Y6, where thermal annealing dramatically changed the TA spectra, particularly in the 700–800 nm region (Figs. 4c and 4d). The positive signal was unclear for the as-cast film, whereas it was distinct after thermal annealing. It is well-known that P3HT shows a PIA of hole polarons at 700 nm and 1000 nm;[50] therefore, the abovementioned band is not attributable to a hole polaron, which supports our attribution of the new PIA to Y6 anions in crystalline domains. Emphatically, a redshift of the Y6 GSB peak was also observed for PTB7-Th and P3HT-based blend films, irrespective of the emergence of the positive PIA at ~800 nm, again indicating that the shift in the GSB peak is independent of the spectral overlap. It is also important to note that the PIA at ~800 nm was observed only in blend films with relatively high EQEs (Figs. S9 and S10). Therefore, we conclude that the emergence of the positive PIA is a sign of efficient FC generation.[18]

Slow yet efficient charge dissociation

Another important finding from Fig. 4d is that the positive PIA observed at ~700–800 nm is unimodal for the P3HT/Y6 blend film, in sharp contrast to the bimodal PIA for the PM6/Y6 blend film (Fig. 3b). This means that the positive PIA at ~680 nm observed in the PM6/Y6 blend film is attributable to a PM6-related signal. As shown in Figs. 5a and 5b, the rise at 680 nm is slightly slower than that at 630 nm (GSB of PM6). The time lag between exciton dissociation and the emergence of the positive PIA at 680 nm is more pronounced at higher excitation fluences, at which the SSA leads to a significantly faster exciton decay (Figs. S26 and S27). Therefore, the attribution of the positive PIA at ~680 nm to the hole polaron of PM6 is inappropriate.

A recent study showed that PM6 exhibits a steady-state EA spectrum in this wavelength region.[51] Therefore, in line with previous studies,[18,42,51,52] this band is attributable to the EA of PM6. When an exciton dissociates to form an electron–hole pair at the D/A interface, the electron–hole pair generates a dipole-like local electric field in the surroundings. This results in a Stark shift in the absorption spectrum, resulting in the addition of a first-derivative-like transient EA to the TA spectra. Note that the positive PIA in the ~800 nm region, which we attribute to Y6 anions in crystalline domains, cannot be assigned to an EA signal of Y6 because no (steady-state) EA peak was reported at ~800 nm for pristine Y6 or PM6/Y6 blend.[52,53] As the EA amplitude depends on the strength of the local electric field, which is a function of the separation distance between the electron and hole, we can directly probe the dissociation kinetics of the electron–hole pair. The fact that the EA signals reached their maximum value slightly after the occurrence of hole transfer, as shown in Fig. 5b, indicates that long-range spatial dissociation of CT states takes place on a time scale of picoseconds (see Fig. S28 for more details).

The situation is completely different after photoexcitation at 600 nm, which mainly excites PM6. As shown in Fig. S29, PM6 excitons dissociate into charges as rapidly as ~0.5 ps. Interestingly, the EA amplitude was already large at 1 ps after photoexcitation and almost unchanged until 100 ps (Figs. 5c-f). As the offset between the excited state energy of PM6 (1.9 eV) and E_{CT} is sufficiently large to access the

delocalized state, this fast dissociation means that electron–hole pairs undergo rapid spatial separation through the delocalized wave function before thermalization, despite the opposing Coulomb attractions, as in the case of previous studies with sufficient energy offset.[26,29] It should be noted that the fast EA rise was not observed in a previous report.[54] We believe this discrepancy is due to differences in domain size. Because the exciton dissociation is slower in ref. 54 probably due to the larger domain size, we expect that energy transfer from PM6 to Y6 will make a larger contribution prior to electron transfer, which decreases the fraction of fast EA rise. These results clearly reveal that the charge dissociation mechanism after the hole transfer is different from that after the electron transfer in the PM6/Y6 blend. However, what is critically important here is that the EA amplitude after hole transfer finally reached its maximum value comparable to that after electron transfer, as shown in Fig. 5f, indicating that there is no apparent difference in FC generation yield between donor and acceptor excitation. This is consistent with the flat EQE spectrum of this device (Fig. S10b), indicating that FC generation yield is independent of the excitation wavelength. Efficient FC generation after Y6 selective excitation is further corroborated by the fact that charge decay dynamics is sensitively dependent on the excitation fluence (Fig. S30), indicating that the bimolecular recombination is the dominant deactivation channel for charges.

Efficient charge dissociation driven by downhill energy relaxation

The time scale of charge dissociation after the hole transfer is ~10 ps, which is too slow to be rationalized by the model proposed for the large offset systems, as discussed in the previous section. On the other hand, this time scale is too fast to be rationalized within the Onsager framework.[20] Interestingly, as shown in Fig. 6a, the time evolution of the EA signals coincides well with that of the Y6 anion in the crystalline domain and the GSB peak shift, suggesting that the slow yet efficient charge dissociation is driven by downhill energy relaxation of charges through cascaded energy landscape near the interface. To confirm this hypothesis, we focus on the temperature dependence of the charge dissociation dynamics, as shown in Fig. 7 (temperature dependence of the TA spectra is found in the Supplementary Information, Figs. S31 and S32). Both the FC generation kinetics and the GSB peak shift were less sensitive to temperature (Figs. 7a and 7b). By applying the Arrhenius fit for the inverse of the rise time constant k_{rise} at 780 nm (Fig. 7c), the activation energy E_a for charge dissociation was determined to be as small as ~4.0–9.4 meV (see Fig. S33 for more details). As a result, the FC generation yield was clearly independent of temperature (Fig. 7d). On the other hand, temperature-dependent FC generation has been reported recently.[53] We believe that the discrepancy arises from a difference in the excitation fluence. A high excitation fluence results in undesirable bimolecular processes such as SSA and bimolecular charge recombination, both of which depend on temperature. We believe that our results are reliable because we maintained the excitation fluence as low as possible. Temperature-insensitive FC generation is consistent with the previously reported temperature-dependence of EQE, wherein the activation energy for the EQE was determined to be as low as 6 meV for the PM6/Y6 device.[17] The authors also performed the time-delayed collection field measurements at various temperatures and observed negligible temperature dependence; thereby, they concluded that the FC generation is temperature independent and the activation energy of the EQE originates from the charge transport issues. The observation that the FC generation yield is insensitive to temperature is again

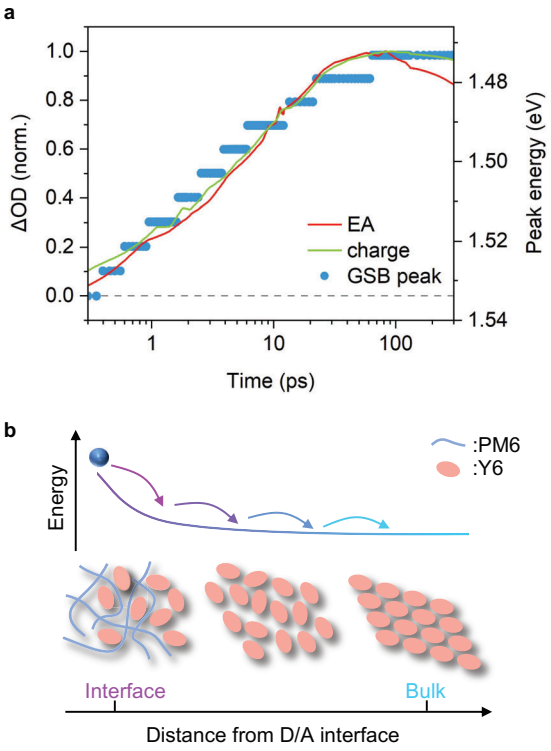

Fig. 6. **a** Correlation between time evolution of EA monitored at 680 nm and crystalline Y6 anion monitored at 760 nm (solid lines, left axis) as well as shift in the peak energy of Y6 GSB in the PM6/Y6 blend film (blue circles, right axis). **b** Schematic showing the relationship between the cascaded energy landscape and the crystallinity of Y6. The coexistence of less-ordered interfacial regions and highly ordered crystalline regions generates the energy cascade near the interface as a key driver for slow yet efficient FC generation.

inconsistent with the Onsager framework but is rationalized by our hypothesis that the charge dissociation is driven by the downhill energy relaxation of charges through the energy cascades generated near the interfaces. Owing to the energy cascade, the Coulomb potential barrier at the interfaces is compensated, resulting in efficient charge dissociation without an activation barrier (Figs. 1a and 6b). This picture also explains the poor FC generation in the D-rich PM6/Y6 and as-cast P3HT/Y6 blend films, wherein Y6 molecules are less aggregated.

The origin of this energy landscape is most likely due to the high crystallinity of Y6. Since the ordered regions are expected to be energetically more stable than at the D/A interfaces for charges, the coexistence of less-ordered interfacial regions and highly ordered crystalline regions generates the energy cascade near the interface.[55–58] Another possible explanation for the origin of the energy cascade is the large quadrupole moment of Y6. Recent studies have highlighted the importance of the quadrupole moment in adjusting the E_{CT} at the interface,[17,38,59] wherein the authors proposed that, since a concentration gradient of Y6 exists near the D/A interface, charge–quadrupole interactions increase continuously with increasing distance from the D/A interface, resulting in the cascaded energy landscape near the D/A interface

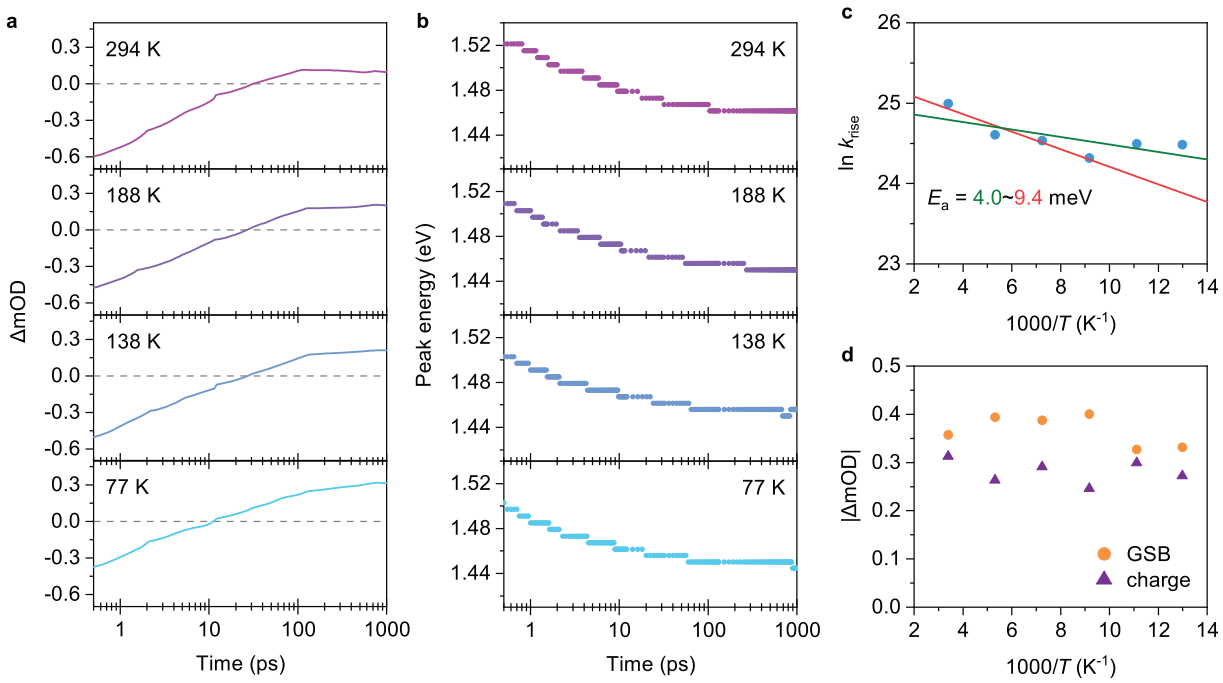

Fig. 7. **a** FC generation kinetics at various temperatures monitored at 780 nm. **b** Shift in the peak energy of Y6 GSB at various temperatures. **c** Arrhenius plot for the inverse of the rise time constant k_{rise} monitored at 780 nm. **d** Arrhenius plot for the TA amplitude at 850 nm (Y6 GSB) and 970 nm (charge). TA signals at 500 ps after photoexcitation are used to reduce the contribution of bimolecular recombination, which should depend on temperature.

(also termed as a bias potential in their reports).[17,38] The fact that there are many examples of offset-less FC generation in A–D–A-type NFA-based OSCs and a few in fullerene-based OSCs also corroborates this hypothesis. It is clear that more effort is necessary to reveal the mechanisms underlying the formation of the energy cascade as well as understanding the desirable interfacial morphology. Nevertheless, the key for efficient FC generation without an energy offset is the presence of an energy difference between the bulk and the D/A interface. Therefore, we propose that a large discrepancy of HOMO (LUMO) energy levels determined in the solution (CV) and solid (PYS or UPS) states can be used for an initial material screening for achieving efficient FC generation with a small voltage loss, because the large discrepancy between CV and PYS/UPS results implies the possibility of forming the desired energy cascade near the interface. It should be noted that the HOMO energy offset determined by CV provides a more reliable measure of V_{OC} loss because the recombination centre is the disordered D/A interface.

Conclusions

The mechanism for efficient offset-less charge separation in a topical PM6/Y6 blend system has only been speculated or reported on the basis of indirect results. This study presents clear, direct experimental evidence for the mechanism underlying FC generation in the PM6/Y6 blend. After the fast hole transfer from Y6 to PM6, despite the small energy offset of ~0.12 eV, slow spatial dissociation of the CT states on a time scale of ~10 ps was observed. This is in sharp contrast to the rapid spatial separation after photoexcitation of PM6, as in the case of previous reports. Importantly, however, the slow FC generation after the hole transfer undergoes as efficient as that after the electron transfer. The activation energy for the slow charge dissociation is as small as ~4.0–9.4 meV, resulting in temperature independent FC generation, even at 77 K. We found that the cascaded energy landscape generated near the interfaces is the key driver for the slow yet efficient FC generation. Since Y6 forms an energetic cascade near the D/A interface, charges can move away from the D/A interface without experiencing the activation barrier because the attracting Coulomb barrier is compensated by the energy cascade. This study highlights the importance of the interfacial energetics for FC generation with small energy offset. Further optimization of the blend morphology will enable completely an offset-less FC generation without any geminate recombination loss.

Finally, future perspectives regarding Y6-based devices are discussed below. An unaddressed challenge regarding Y6-based devices is relatively fast bimolecular recombination loss. In the PM6/Y6 blend film, we observed the remarkable Y6 triplet formation via bimolecular recombination, as shown in Fig. S34. The time constant for back charge transfer from CT to Y6 triplet has recently been reported to be as fast as 10^{11}–10^{12} s^{-1}.[42] This is probably due to the small difference between E_{CT} and the lowest excited triplet state energy E_{T1} of Y6 (Fig. 1b).[39] E_{T1} of Y6 in the solid state was estimated to be between 1.14–1.26 eV, which indicates that E_{T1} is lying just below E_{CT} (1.29 eV). In the Marcus inverted regime, the CT–triplet transition rate scales exponentially with decreasing the energy difference between these states. Thus, the small CT–triplet energy difference results in a fast back charge transfer that forms Y6 triplet excitons at the D/A interfaces, which are then rapidly quenched by

charges (triplet–charge annihilation) or other triplets (triplet–triplet annihilation). This means that the formation of Y6 triplet excitons is a terminal loss process. Therefore, regeneration of CT states from Y6 triplets before deactivation to the ground state will be vital for suppressing the bimolecular recombination loss.

Author Contributions

Y.T. conceived and directed the project. S.N., R.S. and Y.S. performed steady-state and time-resolved optical measurements under the supervision of Y.T. T.S. and R.S. fabricated devices for all photovoltaic measurements. Y.T. developed numerical methods. S.N., T.T., and Y.T. analysed time-resolved data. S.N. and Y.T. prepared the original version of the manuscript. All authors have given approval to the final version of the manuscript.

Conflicts of interest

There are no conflicts to declare.

Acknowledgements

This study was partly supported by JST PRESTO program Grant Number JPMJPR1874, JSPS KAKENHI Grant Numbers 21H02012 and 21H05394, The Murata Science Foundation, The Sumitomo Foundation, and Ogasawara Toshiaki Memorial Foundation.

References

1. J. Hou, O. Inganäs, R. H. Friend and F. Gao, *Nat. Mater.*, 2018, **17**, 119-128.
2. G. Y. Zhang, J. B. Zhao, P. C. Y. Chow, K. Jiang, J. Q. Zhang, Z. L. Zhu, J. Zhang, F. Huang and H. Yan, *Chem. Rev.*, 2018, **118**, 3447-3507.
3. A. Wadsworth, M. Moser, A. Marks, M. S. Little, N. Gasparini, C. J. Brabec, D. Baran and I. McCulloch, *Chem. Soc. Rev.*, 2019, **48**, 1596-1625.
4. A. Karki, A. J. Gillett, R. H. Friend and T. Q. Nguyen, *Adv. Energy Mater.*, 2020, **11**, 2003441.
5. A. Armin, W. Li, O. J. Sandberg, Z. Xiao, L. Ding, J. Nelson, D. Neher, K. Vandewal, S. Shoaee, T. Wang, H. Ade, T. Heumüller, C. Brabec and P. Meredith, *Adv. Energy Mater.*, 2021, **11**, 2003570.
6. Q. Liu, Y. Jiang, K. Jin, J. Qin, J. Xu, W. Li, J. Xiong, J. Liu, Z. Xiao, K. Sun, S. Yang, X. Zhang and L. Ding, *Sci. Bull.*, 2020, **65**, 272-275.
7. F. Liu, L. Zhou, W. Liu, Z. Zhou, Q. Yue, W. Zheng, R. Sun, W. Liu, S. Xu, H. Fan, L. Feng, Y. Yi, W. Zhang and X. Zhu, *Adv. Mater.*, 2021, **33**, 2100830.
8. T. Zhang, C. An, P. Bi, Q. Lv, J. Qin, L. Hong, Y. Cui, S. Zhang and J. Hou, *Adv. Energy Mater.*, 2021, **11**, 2101705.
9. M. Zhang, L. Zhu, G. Zhou, T. Hao, C. Qiu, Z. Zhao, Q. Hu, B. W. Larson, H. Zhu, Z. Ma, Z. Tang, W. Feng, Y. Zhang, T. P. Russell and F. Liu, *Nat. Commun.*, 2021, **12**, 309.
10. J. Yuan, Y. Q. Zhang, L. Y. Zhou, G. C. Zhang, H. L. Yip, T. K. Lau, X. H. Lu, C. Zhu, H. J. Peng, P. A. Johnson, M. Leclerc, Y. Cao, J. Ulanski, Y. F. Li and Y. P. Zou, *Joule*, 2019, **3**, 1140-1151.
11. A. Karki, J. Vollbrecht, A. L. Dixon, N. Schopp, M. Schrock, G. N. M. Reddy and T.-Q. Nguyen, *Adv. Mater.*, 2019, **31**, 1903868.
12. S. M. Hosseini, N. Tokmoldin, Y. W. Lee, Y. Zou, H. Y. Woo, D. Neher and S. Shoaee, *Sol. RRL*, 2020, **4**, 2000498.
13. J. Wu, J. Lee, Y.-C. Chin, H. Yao, H. Cha, J. Luke, J. Hou, J.-S. Kim and J. R. Durrant, *Energy Environ. Sci.*, 2020, **13**, 2422-2430.
14. G. Zhang, X.-K. Chen, J. Xiao, P. C. Y. Chow, M. Ren, G. Kupgan, X. Jiao, C. C. S. Chan, X. Du, R. Xia, Z. Chen, J. Yuan, Y. Zhang, S. Zhang, Y. Liu, Y. Zou, H. Yan, K. S. Wong, V. Coropceanu, N. Li, C. J. Brabec, J.-L. Bredas, H.-L. Yip and Y. Cao, *Nat. Commun.*, 2020, **11**, 3943.
15. N. Tokmoldin, S. M. Hosseini, M. Raoufi, L. Q. Phuong, O. J. Sandberg, H. Guan, Y. Zou, D. Neher and S. Shoaee, *J. Mater. Chem. A*, 2020, **8**, 7854-7860.
16. N. Tokmoldin, J. Vollbrecht, S. M. Hosseini, B. Sun, L. Perdigón-Toro, H. Y. Woo, Y. Zou, D. Neher and S. Shoaee, *Adv. Energy Mater.*, 2021, **11**, 2100804.
17. L. Perdigón-Toro, H. Zhang, A. Markina, J. Yuan, S. M. Hosseini, C. M. Wolff, G. Zuo, M. Stolterfoht, Y. Zou, F. Gao, D. Andrienko, S. Shoaee and D. Neher, *Adv. Mater.*, 2020, **32**, 1906763.
18. A. Karki, J. Vollbrecht, A. J. Gillett, S. S. Xiao, Y. Yang, Z. Peng, N. Schopp, A. L. Dixon, S. Yoon, M. Schrock, H. Ade, G. N. M. Reddy, R. H. Friend and T.-Q. Nguyen, *Energy Environ. Sci.*, 2020, **13**, 3679-3692.
19. L. Q. Phuong, S. M. Hosseini, O. J. Sandberg, Y. Zou, H. Y. Woo, D. Neher and S. Shoaee, *Sol. RRL*, 2021, **5**, 2000649.
20. T. M. Clarke and J. R. Durrant, *Chem. Rev.*, 2010, **110**, 6736-6767.
21. R. A. Janssen and J. Nelson, *Adv. Mater.*, 2013, **25**, 1847-1858.
22. F. Gao and O. Inganäs, *Phys. Chem. Chem. Phys.*, 2014, **16**, 20291-20304.
23. O. Inganäs, *Adv. Mater.*, 2018, **30**, 1800388.
24. Y. Tamai, *Polym. J.*, 2020, **52**, 691-700.
25. A. A. Bakulin, A. Rao, V. G. Pavelyev, P. H. van Loosdrecht, M. S. Pshenichnikov, D. Niedzialek, J. Cornil, D. Beljonne and R. H. Friend, *Science*, 2012, **335**, 1340-1344.
26. S. Gélinas, A. Rao, A. Kumar, S. L. Smith, A. W. Chin, J. Clark, T. S. van der Poll, G. C. Bazan and R. H. Friend, *Science*, 2014, **343**, 512-516.
27. A. C. Jakowetz, M. L. Böhm, J. Zhang, A. Sadhanala, S. Huettner, A. A. Bakulin, A. Rao and R. H. Friend, *J. Am. Chem. Soc.*, 2016, **138**, 11672-11679.
28. A. C. Jakowetz, M. L. Bohm, A. Sadhanala, S. Huettner, A. Rao and R. H. Friend, *Nat. Mater.*, 2017, **16**, 551-557.
29. Y. Tamai, Y. Fan, V. O. Kim, K. Ziabrev, A. Rao, S. Barlow, S. R. Marder, R. H. Friend and S. M. Menke, *ACS Nano*, 2017, **11**, 12473-12481.
30. K. Vandewal, *Annu. Rev. Phys. Chem.*, 2016, **67**, 113-133.
31. M. Azzouzi, T. Kirchartz and J. Nelson, *Trens Chem.*, 2019, **1**, 49-62.
32. K. Vandewal, S. Mertens, J. Benduhn and Q. Liu, *J. Phys. Chem. Lett.*, 2020, **11**, 129-135.
33. T. Saito, S. Natsuda, K. Imakita, Y. Tamai and H. Ohkita, *Sol. RRL*, 2020, **4**, 2000255.
34. M. Wang, H. Wang, T. Yokoyama, X. Liu, Y. Huang, Y. Zhang, T.-Q. Nguyen, S. Aramaki and G. C. Bazan, *J. Am. Chem. Soc.*, 2014, **136**, 12576-12579.
35. K. Kawashima, Y. Tamai, H. Ohkita, I. Osaka and K. Takimiya, *Nat. Commun.*, 2015, **6**, 10085.
36. N. A. Ran, J. A. Love, C. J. Takacs, A. Sadhanala, J. K. Beavers, S. D. Collins, Y. Huang, M. Wang, R. H. Friend, G. C. Bazan and T.-Q. Nguyen, *Adv. Mater.*, 2016, **28**, 1482-1488.
37. S. M. Menke, A. Cheminal, P. Conaghan, N. A. Ran, N. C. Greehnam, G. C. Bazan, T. Q. Nguyen, A. Rao and R. H. Friend, *Nat. Commun.*, 2018, **9**, 277.
38. S. Karuthedath, J. Gorenflot, Y. Firdaus, N. Chaturvedi, C. S. P.

De Castro, G. T. Harrison, J. I. Khan, A. Markina, A. H. Balawi, T. A. D. Peña, W. Liu, R.-Z. Liang, A. Sharma, S. H. K. Paleti, W. Zhang, Y. Lin, E. Alarousu, D. H. Anjum, P. M. Beaujuge, S. De Wolf, I. McCulloch, T. D. Anthopoulos, D. Baran, D. Andrienko and F. Laquai, *Nat. Mater.*, 2021, **20**, 378-384.

39. S. Natsuda, Y. Sakamoto, T. Takeyama, R. Shirouchi, T. Saito, Y. Tamai, H. Ohkita, *J. Chem. Phys. C*, 2021, **125**, 20806-20813.
40. K. Vandewal, K. Tvingstedt, J. V. Manca and O. Inganäs, *IEEE J. Sel. Top. Quantum Electron.*, 2010, **16**, 1676-1684.
41. K. Vandewal, K. Tvingstedt, A. Gadisa, O. Inganäs and J. V. Manca, *Phys. Rev. B*, 2010, **81**, 125204.
42. A. J. Gillett , A. Privitera, R. Dilmurat, A. Karki, D. Qian, A. Pershin, G. Londi, W. K. Myers, J. Lee, J. Yuan, S.-J. Ko, M. K. Riede, F. Gao, G. C. Bazan, A. Rao, T.-Q. Nguyen, D. Beljonne, R. H. Friend, *Nature*, 2021, **597**, 666-671.
43. Y. Tamai, H. Ohkita, H. Benten and S. Ito, *J. Phys. Chem. Lett.*, 2015, **6**, 3417-3428.
44. T. Umeyama, K. Igarashi, D. Sasada, Y. Tamai, K. Ishida, T. Koganezawa, S. Ohtani, K. Tanaka, H. Ohkita and H. Imahori, *Chem. Sci.*, 2020, **11**, 3250-3257.
45. Y. Liu, L. Zuo, X. Shi, A. K. Y. Jen and D. S. Ginger, *ACS Energy Lett.*, 2018, **3**, 2396-2403.
46. A. Karki, J. Vollbrecht, A. J. Gillett, P. Selter, J. Lee, Z. Peng, N. Schopp, A. L. Dixon, M. Schrock, V. Nádaždy, F. Schauer, H. Ade, B. F. Chmelka, G. C. Bazan, R. H. Friend and T.-Q. Nguyen, *Adv. Energy Mater.*, 2020, **10**, 2001203.
47. J. Zhang, W. Liu, G. Zhou, Y. Yi, S. Xu, F. Liu, H. Zhu and X. Zhu, *Adv. Energy Mater.*, 2020, **10**, 1903298.
48. G. Zhou, M. Zhang, Z. Chen, J. Zhang, L. Zhan, S. Li, L. Zhu, Z. Wang, X. Zhu, H. Chen, L. Wang, F. Liu and H. Zhu, *ACS Energy Lett.*, 2021, **6**, 2971-2981.
49. R. A. Marcus, *Rev. Mod. Phys.*, 1993, **65**, 599-610.
50. Y. Tamai, H. Ohkita, M. Namatame, K. Marumoto, S. Shimomura, T. Yamanari and S. Ito, *Adv. Energy Mater.*, 2016, **6**, 1600171.
51. T. F. Hinrichsen, C. C. S. Chan, C. Ma, D. Palecek, A. Gillett, S. Chen, X. Zou, G. Zhang, H. L. Yip, K. S. Wong, R. H. Friend, H. Yan, A. Rao and P. C. Y. Chow, *Nat. Commun.*, 2020, **11**, 5617.
52. P. Wan, X. Chen, Q. Liu, S. Mahadevan, M. Guo, J. Qiu, X. Sun, S.-W. Tsang, M. Zhang, Y. Li, S. Chen, *J. Phys. Chem. Lett.*, 2021, **12**, 10595-10602.
53. C. C. S. Chan, C. Ma, X. Zou, Z. Xing, G. Zhang, H.-L. Yip, R. A. Taylor, Y. He, K. S. Wong, P. C. Y. Chow, *Adv. Funct. Mater.*, 2021, **31**, 2107157
54. R. Wang, C. Zhang, Q. Li, Z. Zhang, X. Wang, M. Xiao, *J. Am. Chem. Soc.*, 2020, **142**, 12751-12759.
55. S. Shoaee, S. Subramaniyan, H. Xin, C. Keiderling, P. S. Tuladhar, F. Jamieson, S. A. Jenekhe and J. R. Durrant, *Adv. Funct. Mater.*, 2013, **23**, 3286-3298.
56. Y. Tamai, K. Tsuda, H. Ohkita, H. Benten and S. Ito, *Phys. Chem. Chem. Phys.*, 2014, **16**, 20338-20346.
57. S. Sweetnam, K. R. Graham, G. O. N. Ndjawa, T. Heumueller, J. A. Bartelt, T. M. Burke, W. Li, W. You, A. Amassian and M. D. McGehee, *J. Am. Chem. Soc.*, 2014, **136**, 14078-14088.
58. H. Cha, G. Fish, J. Luke, A. Alraddadi, H. H. Lee, W. Zhang, Y. Dong, S. Limbu, A. Wadsworth, I. P. Maria, L. Francàs, H. L. Sou, T. Du, J.-S. Kim, M. A. McLachlan, I. McCulloch and J. R. Durrant, *Adv. Energy Mater.*, 2019, **9**, 1901254.
59. M. Schwarze, K. S. Schellhammer, K. Ortstein, J. Benduhn, C. Gaul, A. Hinderhofer, L. Perdigón Toro, R. Scholz, J. Kublitski, S. Roland, M. Lau, C. Poelking, D. Andrienko, G. Cuniberti, F. Schreiber, D. Neher, K. Vandewal, F. Ortmann and K. Leo, *Nat. Commun.*, 2019, **10**, 2466.

Supplementary Information for

Cascaded energy landscape as a key driver for slow yet efficient charge separation with small energy offset in organic solar cells

Shin-ichiro Natsuda[1], *Toshiharu Saito*[1], *Rei Shirouchi*[1], *Yuji Sakamoto*[1], *Taiki Takeyama*[1], *Yasunari Tamai*[1,2*], *Hideo Ohkita*[1]

[1] Department of Polymer Chemistry, Graduate School of Engineering, Kyoto University, Katsura, Nishikyo, Kyoto 615-8510, Japan

[2] Japan Science and Technology Agency (JST), PRESTO, 4-1-8 Honcho Kawaguchi, Saitama 332-0012, Japan

[*]to whom correspondence: tamai@photo.polym.kyoto-u.ac.jp

Table of Contents

Experimental details

Film preparation

Films for all spectroscopic measurements were prepared on quartz substrates, which were sequentially cleaned by sonication in toluene, acetone, and ethanol for 15 min each. The optimized PM6/Y6 and PTB7-Th/Y6 blends (1:1.2 w/w, total concentration of 17.6 mg mL^{-1}) were dissolved in chloroform with 0.5 vol% chloronaphthalene as an additive and left to stir at room temperature overnight. Thin films were spin-coated onto the cleaned substrates in a N_2-filled glovebox and then thermally annealed at 110 °C for 5 min. Similarly, the P3HT/Y6 blend (1:1.2 w/w, total concentration of 17.6 mg mL^{-1}) was dissolved in chloroform, but without any additives. It was also stirred at room temperature overnight and spin-coated in the glovebox and then thermally annealed at 140 °C for 10 min. The D-rich PM6/Y6 blend was prepared by the same method as the optimized PM6/Y6 blend, but with a D/A blend ratio of 95:5 (w/w, total concentration of 40 mg mL^{-1}). For TA measurements, the samples were encapsulated in the glovebox.

Device fabrication

Photovoltaic devices were fabricated on ITO/glass substrates (Geomatec Co., 1006, 10 Ω $sq.^{-1}$), which were sequentially cleaned by sonication in toluene, acetone, and ethanol for 15 min each, followed by UV-O_3 treatment (Nippon Laser and Electronics Lab.) for 30 min. PEDOT:PSS (Clevios, Al4083) was spin-coated onto the substrates (~30 nm) and dried on a hot plate (150 °C, 20 min) under ambient conditions. Thereafter, the aforementioned active layers were spin-coated in the glovebox under the same conditions. Subsequently, PDINO was spin-coated from a methanol solution (2 mg mL^{-1}), and ~80 nm of Al was thermally evaporated onto the PDINO layer. The devices were placed in a N_2-filled chamber for *J*–*V*, EQE and EL measurements.

Steady-state absorption and emission spectra

UV–visible absorption spectra were acquired using a UV–visible spectrometer (Hitachi, U-4100). The PL spectra were measured using a fluorescence spectrophotometer (Horiba Jobin Yvon, NanoLog) equipped with a photomultiplier tube (Hamamatsu, R928P) and a liquid-N_2-cooled InGaAs near-IR array detector (Horiba Jobin Yvon, Symphony II). The excitation wavelength was set to 790 nm. The EL spectra were measured using the same setup with a DC voltage and current source/monitor (Advantest, R-6243).

J–V and EQE measurements

The *J–V* characteristics were measured using a DC voltage and current source/monitor (Keithley, 2611B) in the dark and under AM1.5G simulated solar illumination at 100 mW cm^{-2}. The light intensity was corrected using a calibrated Si photodiode (Bunko-Keiki, BS-520). The EQE spectra were measured using a spectral response measurement system (Bunko-Keiki, ECT-25D).

CV

Materials were dissolved in acetonitrile/*o*-dichlorobenzene (9:1 v/v) solutions with 0.1 M tetrabutylammonium perchlorate as the supporting electrolyte. CV measurements were performed using a potentiostat (Princeton Applied Research, Potentiostat/Galvanostat Model 273A) at a scanning rate of 5 mV s^{-1}. A Pt mesh, a Ag/AgCl wire, and a thinly sliced ITO substrate were used as the counter, reference, and working electrode, respectively. Ferrocene was used as an internal reference. The HOMO energies were then evaluated from the onset potential of the first oxidation peak φ_{OX} as $E_{HOMO} = -(\varphi_{OX} + 4.8 - \varphi_{Fe/Fe+})$, where $\varphi_{Fe/Fe+}$ is the redox potential of ferrocene/ferrocenium.

PYS

The IEs were measured using a photoelectron yield spectrometer (Riken Keiki, AC-3) with a power setting of 5 nW. Calibration was performed using an Au layer. All films were prepared on ITO/glass substrates. The threshold energy for the photoelectron emission was evaluated on the basis of the cubic root of the photoelectron yield plotted against the incident photon energy.

TRPL measurements

The TRPL spectra and PL decay kinetics were measured by the time-correlated single-photon-counting (TCSPC) method (Unisoku Scientific Instruments, LSP-200T-VN-EM) with an excitation wavelength of 660 nm. The full width at half maximum of the instrument response function (IRF) is 160 ps. Decay time constant was analyzed by deconvoluting the observed decay with the IRF and an exponential function with a constant fraction.

TA measurements

Femtosecond TA data were collected using a pump and probe femtosecond TA spectroscopy system, which consisted of a TA spectrometer (Ultrafast Systems, Helios) and a regenerative amplified Ti:sapphire laser

(Spectra-Physics, Hurricane). A fundamental pulse with a wavelength of 800 nm was used as the excitation source for Y6, whereas it was converted with an ultrafast optical parametric amplifier (Spectra-Physics, TOPAS) for excitation wavelength dependence measurements. The TA data were collected over a time range from −5 ps to 3 ns. The temperature dependence was measured using a liquid-N_2-cooled cryostat (Oxford Instruments, Optistat DN-V).

The microsecond TA data were collected using a sensitive microsecond TA system. A Nd:YAG laser (Elforlight, SPOT-10-200-532) operating at a wavelength of 532 nm was used as the excitation source. White light from a tungsten lamp with a stabilized power source was used as the probe light. Two monochromators and appropriate optical cut-off filters were placed before and after the sample to increase the signal-to-noise ratio (SNR). Further details of our TA setup have been presented elsewhere.[S1]

TA data processing

TA data were denoised by total variation (TV) regularization method to increase SNR. Details of this method are described in the "TA data processing via total variation regularization" section.

DFT calculations

DFT calculations were performed for model compounds of isolated PM6 dimer and Y6, wherein alkyl side chains were shortened to reduce the computational effort, using the Gaussian 16 rev. A package.[S2] In order to obtain the reorganization energy, these molecules were first optimized in the ground state using the B3LYP functional and 6-311G(d,p) basis set. Second, the positively charged PM6 dimer and negatively charged Y6 were optimized using the 6-31G(d) and 6-31+G(d) basis sets, respectively. Third, time-dependent (TD)-DFT with B3LYP/6-31+G(d) was carried out to optimize Y6 in the singlet excited state. Finally, the positively charged PM6 dimer in the ground state geometry and negatively charged Y6 in the excited state geometry were calculated using the 6-31G(d) and 6-31+G(d) basis sets, respectively. The reorganization energy was then obtained from the difference of the total energy between participants.

Absorption and PL spectra of pristine PM6 and Y6 films

E_{S1} for pristine PM6 and Y6 films was determined to be 1.90 and 1.39 eV, respectively, from the intersection of the absorption and PL spectra.

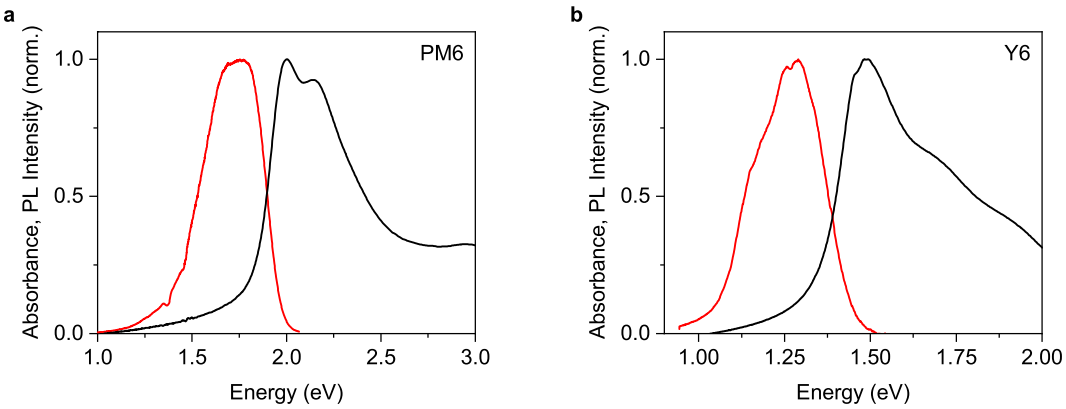

Fig. S1. Absorption (black) and PL (red) spectra of pristine (**a**) PM6 and (**b**) Y6 films.

EQE and EL spectra of the optimized PM6/Y6 blend

E_{S1} for the optimized PM6/Y6 blend was determined to be 1.41 eV from the intersection of the EQE and EL spectra.

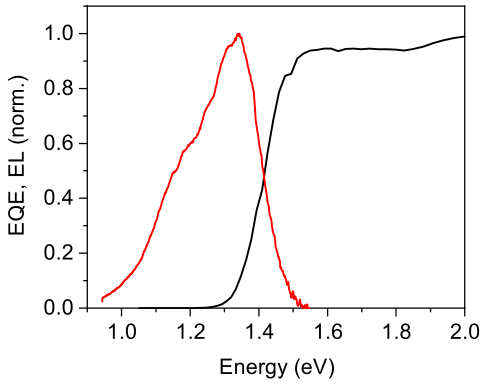

Fig. S2. EQE (black) and EL (red) spectra of the optimized PM6/Y6 blend device.

Absorption spectra of PTB7-Th/Y6 and P3HT/Y6 blend films

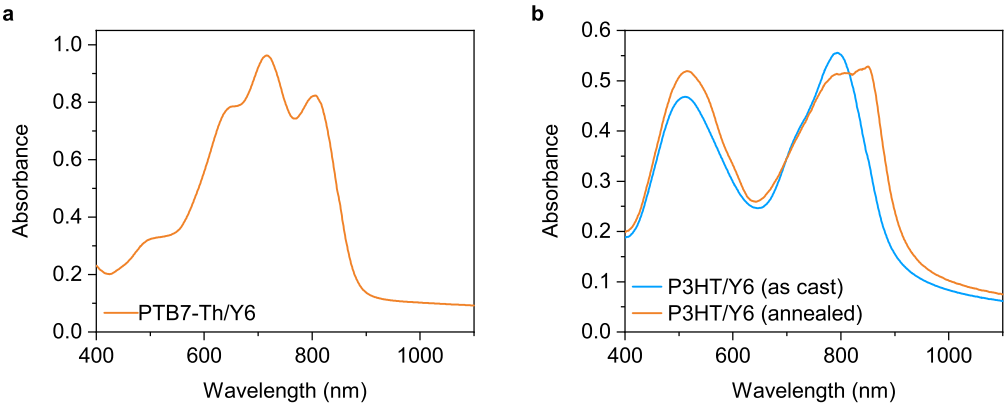

Fig. S3. **a** Absorption spectrum of the PTB7-Th/Y6 blend film. **b** Absorption spectra of the P3HT/Y6 blend film measured before and after thermal annealing at 140 °C for 10 min.

Absorption spectrum of the D-rich PM6/Y6 blend film

The red line in Fig. S4 shows the absorption spectrum of the D-rich PM6/Y6 blend film (95:5 w/w). The peak wavelength corresponding to Y6 absorption in the D-rich blend was clearly blueshifted relative to that of the optimized PM6/Y6 blend film (1:1.2 w/w), indicating that Y6 is more disordered in the D-rich film than that in the optimized blend.

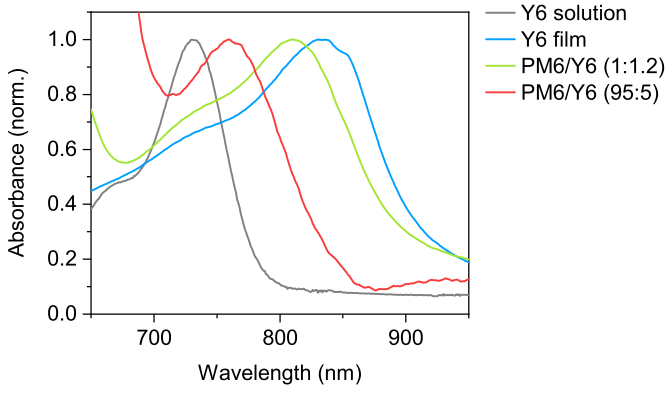

Fig. S4. Absorption spectrum of the D-rich PM6/Y6 blend film (red). Absorption spectra of the optimized PM6/Y6 blend (1:1.2 w/w, green) as well as pristine Y6 in the solution (grey) and solid states (blue) are also shown as references.

PL quenching

The PL quenching yield was defined as the PL intensity ratio, which was ~97%, >99%, and >99% for the PM6/Y6, PTB7-Th/Y6, and P3HT/Y6 blend films, respectively (Fig. S5), indicating that almost all Y6 excitons generated in these blend films dissociate into charges. Previous studies have revealed that Y6 forms crystalline domains as large as 20–30 nm in the PM6/Y6 blends.[S3-S5] Such large domains sometimes result in inefficient charge generation because some excitons cannot reach the D/A interface; however, the PL quenching efficiency of ~97% indicates that almost all Y6 excitons can reach the interface and undergo hole transfer. We previously determined the diffusion constant for Y6 singlet excitons to be 2.1×10^{-2} cm^2 s^{-1},[S6] which corresponds to a mean free path L_D, defined as $L_D = (6D\tau)^{0.5}$, where D is the diffusion constant of Y6 excitons and τ is the exciton lifetime in the blend film (~6.0 ps), of Y6 singlet excitons in the blend film of ~8.7 nm. This indicates that even the excitons generated at the center of the Y6 domain can reach the D/A interface owing to the fast exciton diffusion. On the other hand, the high PL quenching efficiency also implies that almost all charges in the PM6/Y6 blend film decay nonradiatively to the ground state. Recently, Gillett et al. reported that ~90% of the charges decay through the formation of non-emissive Y6 triplet excited states.[S7] Therefore, there is still considerable room to further reduce the voltage loss incurred by nonradiative charge recombination.

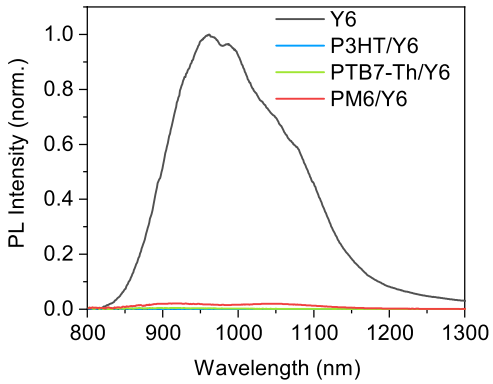

Fig. S5. PL spectra of PM6/Y6 (red), PTB7-Th/Y6 (green), and P3HT/Y6 (blue) blend films, as well as that of a pristine Y6 film (black). The PL intensities were corrected for differences in absorbance at the excitation wavelength of 790 nm.

Marcus fitting

Fig. S6a shows the normalized PL spectra of the PM6/Y6 and PTB7-Th/Y6 blend films as well as that of the pristine Y6 film. Compared to the pristine Y6 film, the PM6/Y6 blend film exhibited a more pronounced PL band at ~1050 nm. Interestingly, this band was not observed for the PTB7-Th/Y6 blend film, indicating that the attribution of this band to a vibronic band of Y6 fluorescence is inappropriate (although there should be some overlap of the vibronic sub-band of Y6 fluorescence as well). Fig. S7a shows the TRPL spectra of the PM6/Y6 blend film. As mentioned in the main text, the PM6/Y6 blend exhibits a longer decay component peaking at ~1050 nm. Therefore, the PL band peaking at ~1050 nm in Fig. S6a can be attributable to the CT emission; this assignment is consistent with a previous report, wherein the authors extracted the CT emission by comparing the PL and EL spectra.[S8]

As shown in Fig. S6c, the CT emission part of the reduced PL spectrum I_{PL}/E can be fitted by a Gaussian function (Equation S1),[S9,S10] where λ, k_B, and T are the reorganization energy, the Boltzmann constant, and absolute temperature, respectively. The parameter f is proportional to the square of the electronic coupling matrix element. From the fitting, E_{CT} was determined to be 1.29 eV. We also applied the same fitting to the TRPL spectrum and obtained E_{CT} of 1.30 eV (Fig. S7b). These values are very close to a recently reported E_{CT} of 1.27 eV determined by EA spectroscopy.[S11]

$$\frac{I_{\mathrm{PL/EL}}}{E} = \frac{f}{\sqrt{4\pi\lambda k_{\mathrm{B}}T}} \exp\left[-\frac{(E_{\mathrm{CT}} - \lambda - E)^2}{4\lambda k_{\mathrm{B}}T}\right] \quad \text{(S1)}$$

Fig. S6b shows the normalized EL spectra of the PM6/Y6 and PTB7-Th/Y6 devices as well as that of a pristine Y6 device. The PTB7-Th/Y6 device showed a clear CT emission at ~1110 nm. In contrast, a superposition of the locally-excited (LE) and CT emissions was observed in the PM6/Y6 device, indicating that E_{CT} is slightly higher in energy in the PM6/Y6 blend than in the PTB7-Th/Y6 blend. The absence of the clear CT emission peak in the EL spectrum of the PM6/Y6 device may be because the repopulation of the LE state is more efficient under a forward bias than that in the PL condition (no applied bias). Although the CT emission is less distinct than that in the PL spectrum, we also performed the same fitting on a shoulder at ~1050 nm, yielding somewhat larger E_{CT} of 1.44 eV (Fig. S6d). Because the CT emission is more distinct in the PL spectrum than in the EL spectrum, we believe that E_{CT} evaluated from the PL spectrum should be more reliable. However, since some uncertainties remain, such as the effect of overlap with the Y6 fluorescence, we use E_{CT} of 1.29 eV with a caveat that this value is an estimate only.

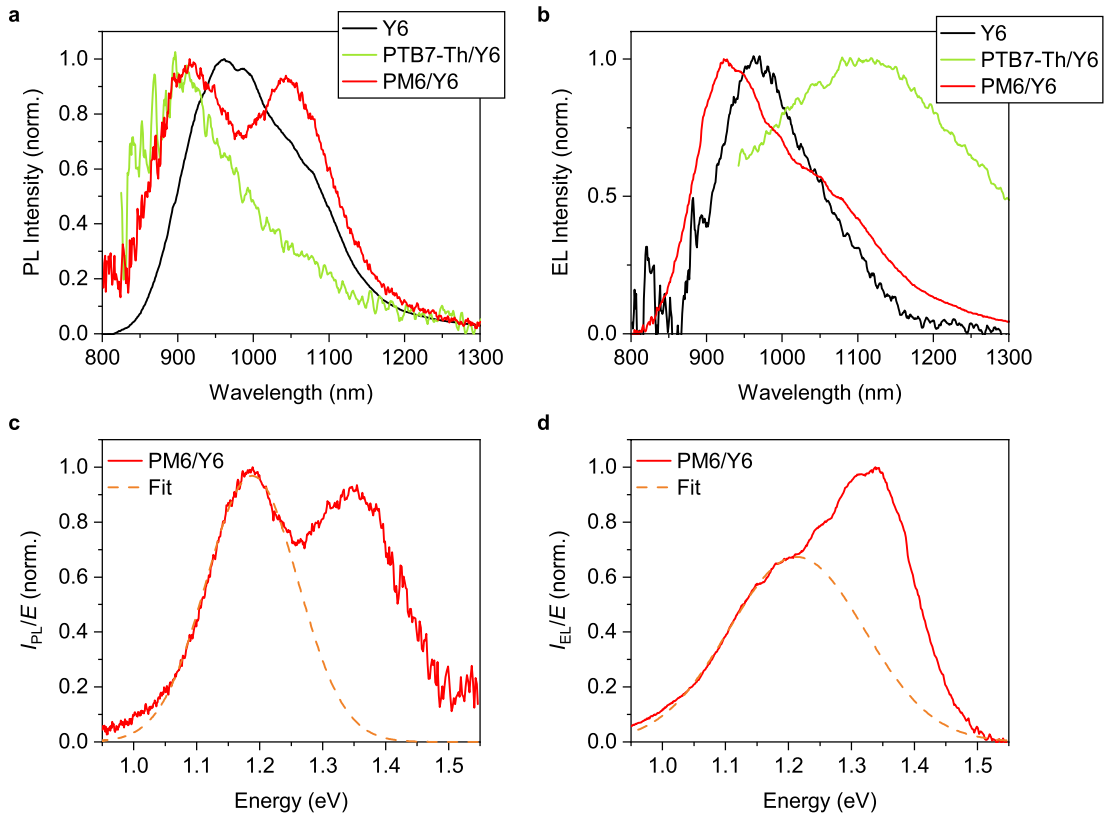

Fig. S6. **a** Normalized PL spectra. **b** Normalized EL spectra. **c** Reduced PL spectrum for the PM6/Y6 blend and **d** reduced EL spectrum for the PM6/Y6 device. Broken lines in (**c**) and (**d**) represent the best fitting curves obtained using a Gaussian function (Equation S1). Note that the emissions from the P3HT/Y6 blends were too weak to be detected.

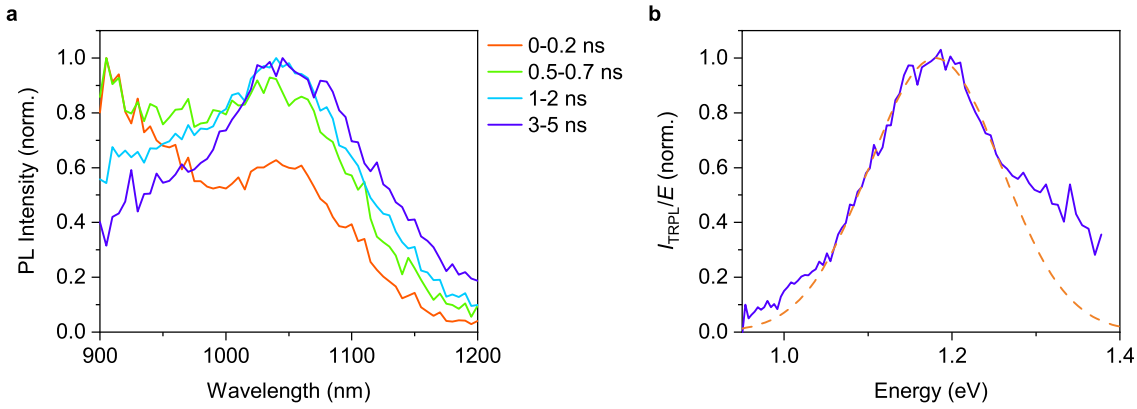

Fig. S7. **a** The TRPL spectra of the PM6/Y6 blend film. **b** Reduced TRPL spectrum for the PM6/Y6 blend (3–5 ns) The broken line represents the best fitting curve obtained using a Gaussian function (Equation S1).

Cyclic voltammetry

The HOMO energies in the solution state were evaluated using CV to be −5.23 and −5.38 eV for PM6 and Y6, respectively. These values are slightly shallower than those previously reported.[S12] This is probably due to the difference in the scanning rate of the CV measurements because scanning too fast may overestimate the onset value. We measured cyclic voltammograms as slowly as possible (5 mV s^{-1}) to approach the reversible condition.[S13] It should be emphasized that what is important here is the relative difference in the HOMO energies between PM6 and Y6. The HOMO energy difference was only 0.15 eV and the small HOMO offset obtained from CV is consistent with previous reports.[S12]

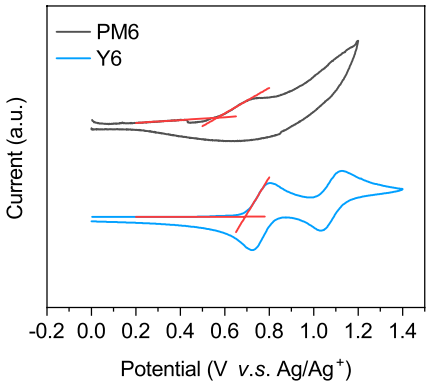

Fig. S8. Cyclic voltammograms of PM6 (black) and Y6 (blue). The HOMO energies were evaluated to be −5.23 eV (PM6) and −5.38 eV (Y6) from the onset determined from the intersection of the two tangents (red lines) for the first oxidation peak. Ferrocene was used as an internal reference.

Photoelectron yield spectroscopy

The IE in the solid state were determined using PYS to be −5.24 and −5.76 eV for PM6 and Y6, respectively, which indicates the presence of a large HOMO energy offset in the solid state. This result agrees with that of Karuthedath et al.[S14]

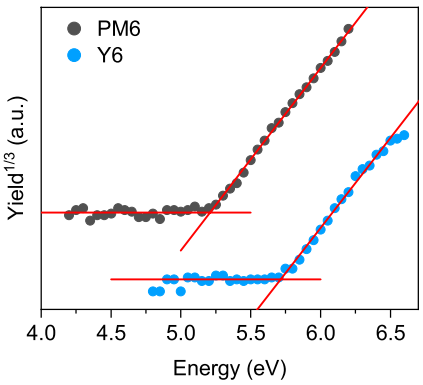

Fig. S9. Photoelectron yield spectra of pristine PM6 (black) and Y6 (blue) films.

Device performance

Fig. S10 shows the *J*–*V* characteristics and the EQE spectrum of the optimized PM6/Y6 device. Our devices reproduce the *J*–*V* characteristics in previous reports.

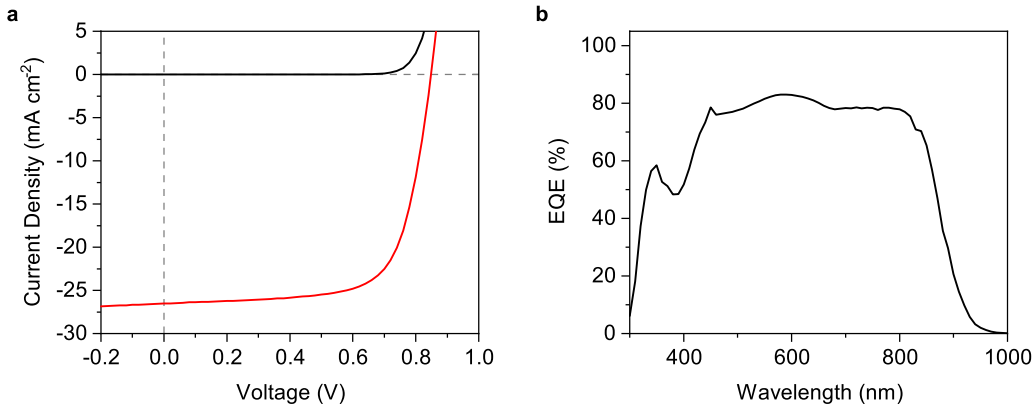

Fig. S10. **a** *J*–*V* characteristics of a PM6/Y6 device measured in the dark (black) and under simulated AM1.5G illumination (100 mA cm^{-2}, red). The device parameters are summarized in Table S1. **b** EQE spectrum of the same device.

Table S1. *J*–*V* characteristics of the PM6/Y6 device

J_{SC} (mA cm^{-2})	$J_{SC}^{calc.\ a}$ (mA cm^{-2})	V_{OC} (V)	FF	PCE (%)
26.5	25.0	0.848	0.703	15.8

[a.] J_{SC} calculated by integrating the EQE spectrum

Device performance of other blends

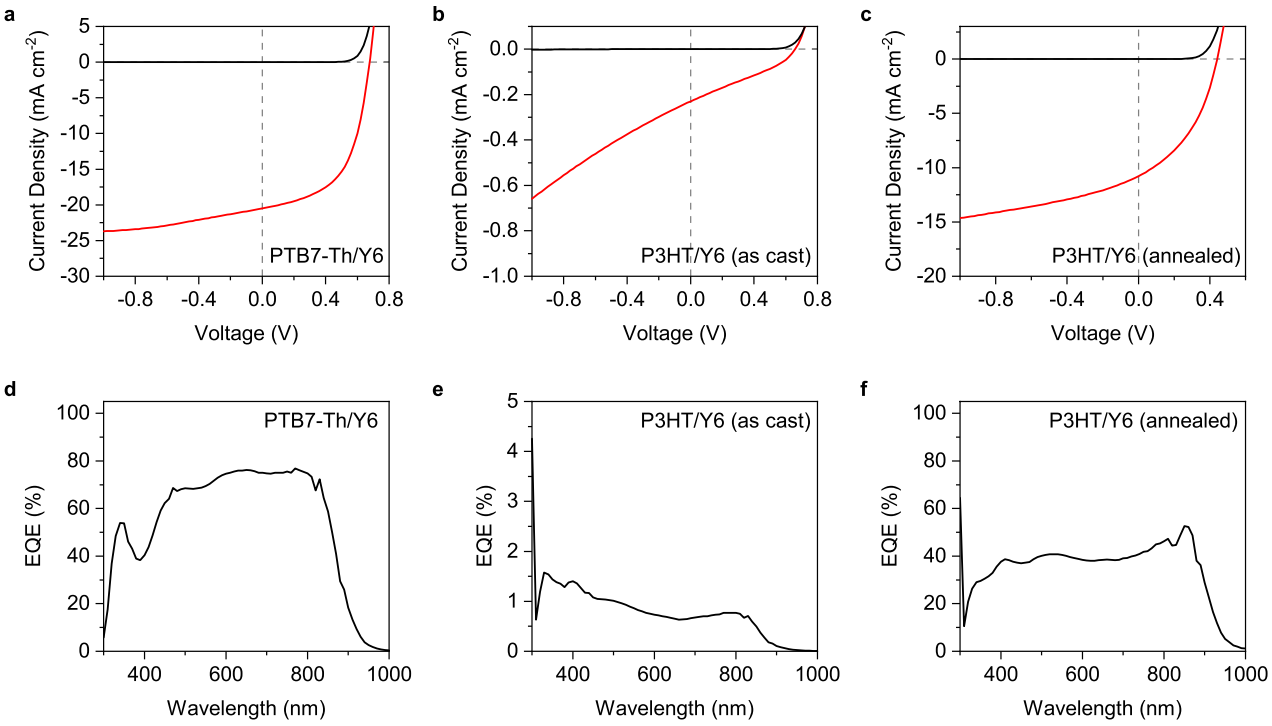

Fig. S11. *J–V* characteristics of (**a**) PTB7-Th/Y6, (**b**) as-cast P3HT/Y6, and (**c**) annealed P3HT/Y6 devices measured in the dark (black) and under simulated AM1.5G illumination (100 mA cm^{-2}, red). The device parameters are summarized in Table S2. EQE spectra of (**d**) PTB7-Th/Y6, (**e**) as-cast P3HT/Y6, and (**f**) annealed P3HT/Y6 devices.

Table S2. *J–V* characteristics of the PTB7-Th/Y6 and P3HT/Y6 devices

Sample	J_{SC} (mA cm^{-2})	$J_{SC}^{calc.\ a}$ (mA cm^{-2})	V_{OC} (V)	FF	PCE (%)
PTB7-Th/Y6	20.8	22.7	0.675	0.533	7.5
P3HT/Y6 (as-cast)	~0.22	~0.26	0.652	0.301	~0.04
P3HT/Y6 (annealed)	10.1	14.1	0.413	0.403	1.7

[a.] J_{SC} calculated by integrating the EQE spectrum

Assignments of the TA spectra

Fig. S12 summarizes the assignments of the TA spectra. Here, we provide details of these assignments.

As we previously reported, Y6 singlet excitons exhibit a sharp PIA band at ~930 nm, a broad PIA tail above 1200 nm, and GSB at 850 nm (Fig. S13). The singlet PIA and GSB are redshifted compared with that of the PM6/Y6 blend film, as discussed in detail in the main text.

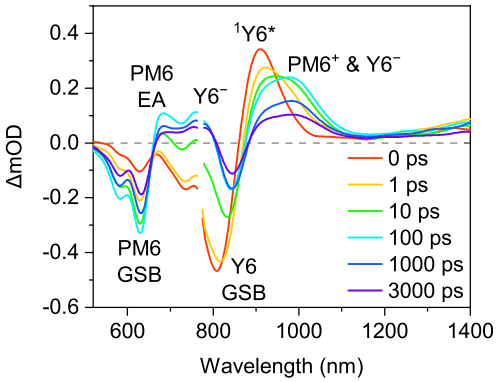

Fig. S12. Summary of assignments of the TA spectra. $^1Y6^*$: singlet excitons of Y6, $Y6^-$: anions of Y6, Y6 GSB: ground-state bleaching of Y6, $PM6^+$: hole polarons of PM6, PM6 GSB: ground-state bleaching of PM6, and PM6 EA: transient electroabsorption of PM6.

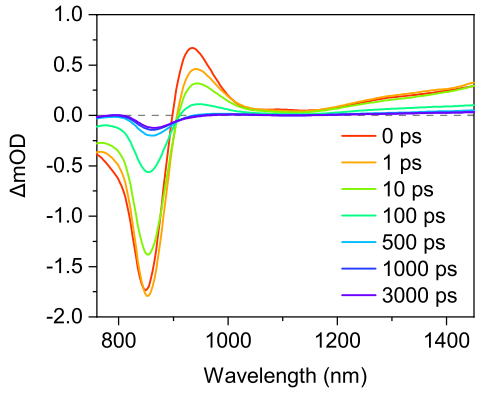

Fig. S13. TA spectra of a pristine Y6 film. The excitation wavelength was 800 nm with a fluence of 3.8 μJ cm^{-2}. Reprinted with permission from ref. S6. Copyright 2021 American Chemical Society.

The long-lived PIA bands in Fig. 3 are still observed on the microsecond time scale except for the positive signals at 680 nm (Fig. S14a). The absence of the 680 nm signal on microsecond time scale is consistent with our assignment of this signal to be attributable to EA due to dipole-like local electric field generated by electron–hole pairs at the interfaces because there exist no CT states on microsecond time scale. At the same

time, this finding also suggests that the 780 nm band is not attributable to EA of Y6. The existence of the positive signals at 780 nm and 960 nm on the microsecond time scale indicates that these bands can be attributable to charged species because Y6 triplet excitons exhibits a PIA band at ~1400 nm.[S6,S7]

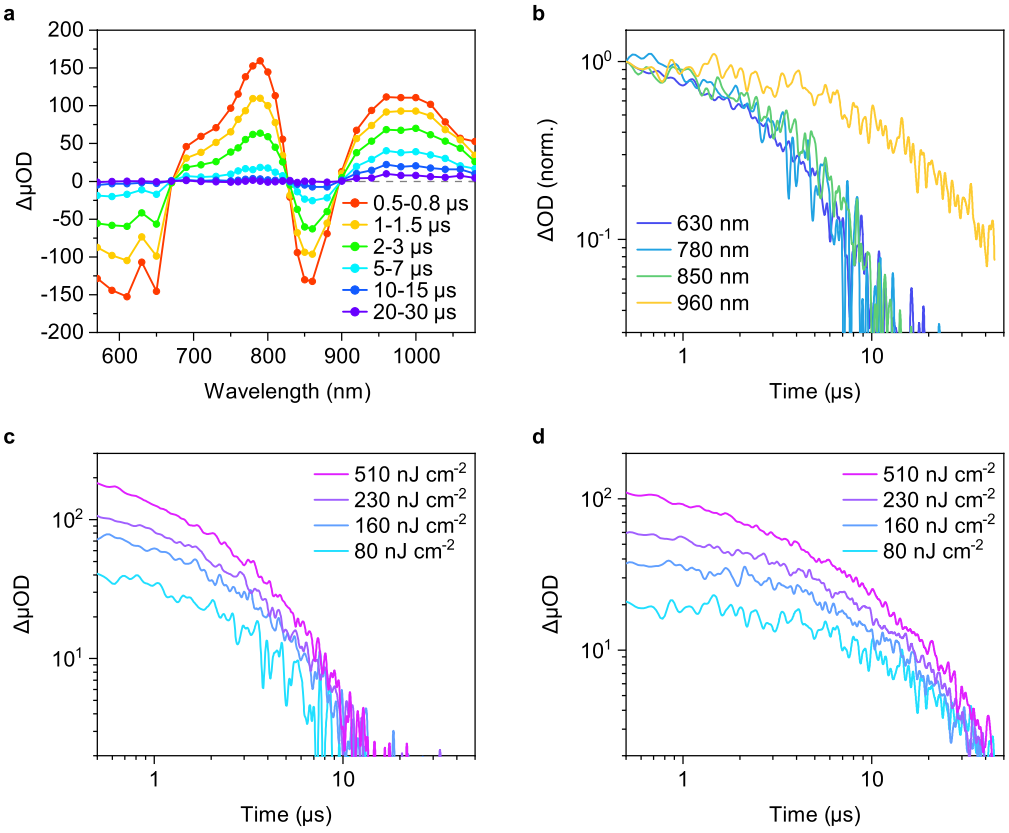

Fig. S14. **a** TA spectra of the PM6/Y6 blend film on the microsecond time scale. The excitation wavelength was 532 nm with a fluence of 510 nJ cm^{-2}. **b** Normalized time evolution of TA signals monitored at four characteristic wavelengths with a fluence of 80 nJ cm^{-2}. **c**,**d** Excitation-fluence dependence of TA decays monitored at (**c**) 780 nm and (**d**) 960 nm.

Here, we provide some additional evidence for the assignments of TA spectra.

Fig. S15 shows the TA spectra of a PM6/PCBM blend film. The TA spectra of a pristine PM6 film is also shown as a reference (broken line). For the pristine PM6 film, a large PIA band at ~1200 nm was observed immediately after photoexcitation, which can be assigned to singlet excitons of PM6.[S15,S16] The singlet excitons monitored at 1200 nm decayed rapidly in the blend film, whereas a new PIA band at ~900 nm was also observed, which is assigned to PM6 hole polarons.[S15,S16]

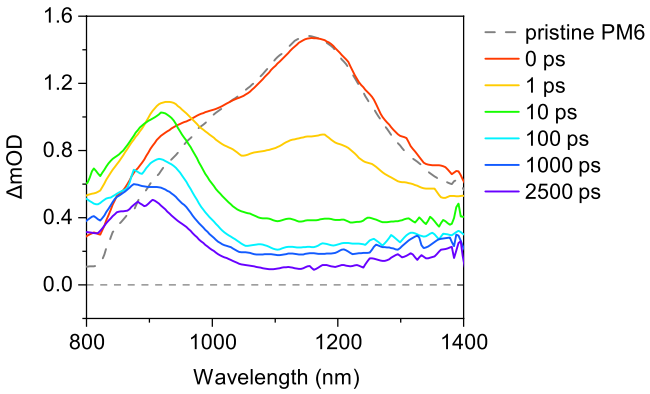

Fig. S15. TA spectra of a PM6/PCBM blend film and a pristine PM6 film as a reference. The excitation wavelength was 590 nm with a fluence of 7.1 μJ cm^{-2}.

Interestingly, the PIA band at ~970 nm in the PM6/Y6 blend film extends into the longer wavelength region and approaches ~1100 nm, suggesting that the Y6 anion PIA band overlaps in this region. To confirm this, we show the TA spectra of the PTB7-Th/Y6 blend film since PTB7-Th hole polarons do not exhibit strong PIA in the 900–1000 nm region.[S17] Fig. S16a shows the TA spectra of the PTB7-Th/Y6 blend film excited at 800 nm. Immediately after photoexcitation, Y6 singlet excitons and GSB bands were observed, as in the case of the PM6/Y6 blend film. Then, the hole polarons and GSB of PTB7-Th, peaking at ~1150 nm and ~730 nm, respectively,[S17] increased rapidly, indicating hole transfer from Y6 to PTB7-Th. A PIA band similar to that of the PM6/Y6 blend in the 900–1000 nm region decayed together with the PTB7-Th hole polaron on later time scale, indicating that this PIA is attributable to Y6 anion. Therefore, the broad PIA peaking at ~970 nm observed in the PM6/Y6 blend film is a superposition of PM6 hole polaron and Y6 anion.

The positive PIA at 780 nm was also observed for the PTB7-Th/Y6 and annealed P3HT/Y6 films all the way from the picosecond time scale to the microsecond time scale, as shown in Figs. S16–S18. The observation of this band in all three blend films (PM6/Y6, PTB7-Th/Y6, and annealed P3HT/Y6) on the microsecond time scale is clear evidence that this band is attributable to Y6 anions. Because this band is not observed in the as-cast P3HT/Y6 blend film, the 780 nm band can be attributable to Y6 anions in the crystalline domains. This assignment is further supported by the bimodal charge decay dynamics observed for the PM6/Y6 blend film, as shown in Fig. S14b. Interestingly, TA signals at 960 nm decay more slowly than those at 780 nm (Fig. S14b). Such bimodal charge-transport behaviour has been observed in other OSCs.[S18] In line with previous reports, the slow decay at 960 nm is a sign that charges in relatively disordered regions are responsible for the PIA at 960 nm, where charges are trapped at shallow trap sites. Since the decay at 780 nm coincides well with the

GSB signals at 630 and 850 nm, the TA signal at 780 nm is responsible for charge transport, i.e., the 780 nm band can be attributable to Y6 anions in crystalline domains; hence, this band is more important than that at 960 nm in terms of FC generation.

Note that for the PTB7-Th/Y6 blend film the 780 nm band cannot be attributed to the EA of PTB7-Th because it shows a peak wavelength at ~740 nm.[S17] On the other hand, the absorption edge of the PTB7-Th hole polaron is observed at this wavelength, which is the reason for the complex (three exponential function) time evolution of this band for the PTB7-Th/Y6 blend film, as discussed in the next section.

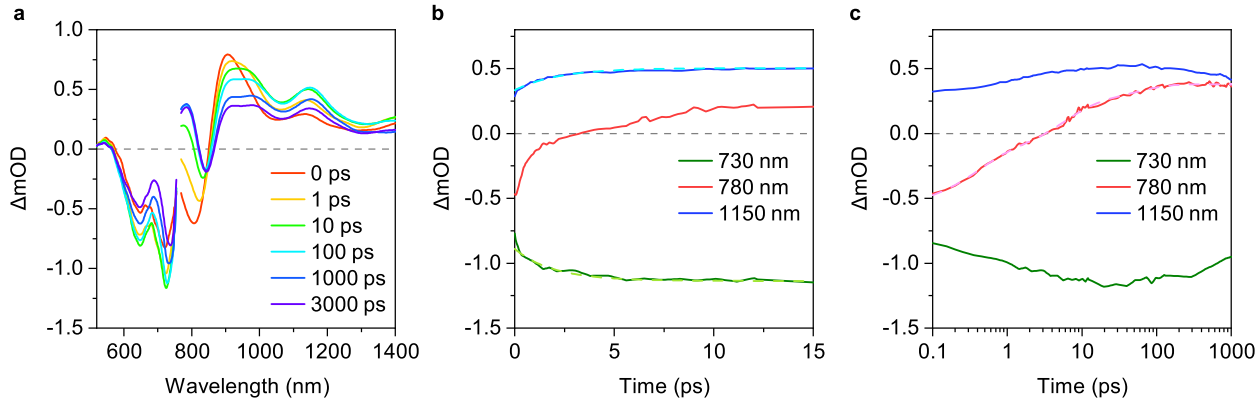

Fig. S16. **a** TA spectra of the PTB7-Th/Y6 blend film. The excitation wavelength was 800 nm with a fluence of 2.4 μJ cm^{-2}. **b** Time evolution of TA signals on an early time scale. Colored broken lines represent the best fit curves by a sum of an exponential function and a constant fraction. **c** Time evolution of TA signals on a later time scale. The coloured broken line represents the best fit curves by a sum of three exponential functions and a constant fraction. Each time constant (fraction) was 0.37 ps (40.5%), 5.4 ps (41.7%), and 51.1 ps (17.8%).

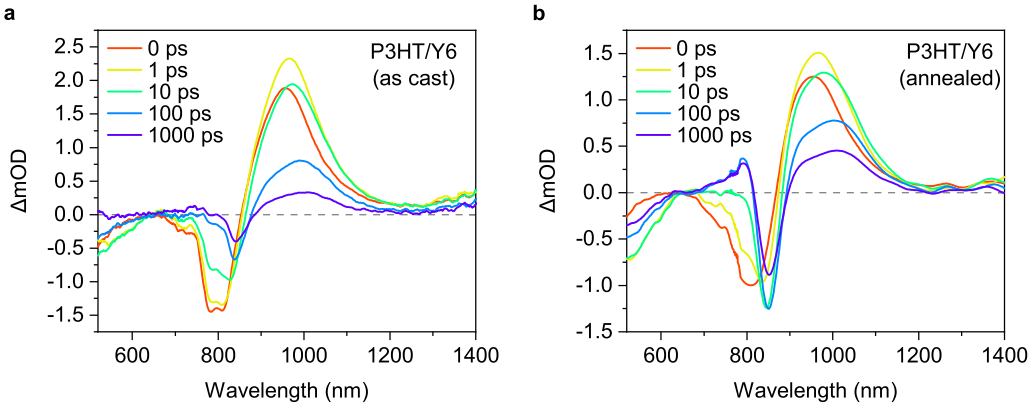

Fig. S17. TA spectra of (**a**) as-cast and (**b**) annealed P3HT/Y6 blend films. The excitation wavelength was 800 nm with a fluence of 5.5 μJ cm^{-2}.

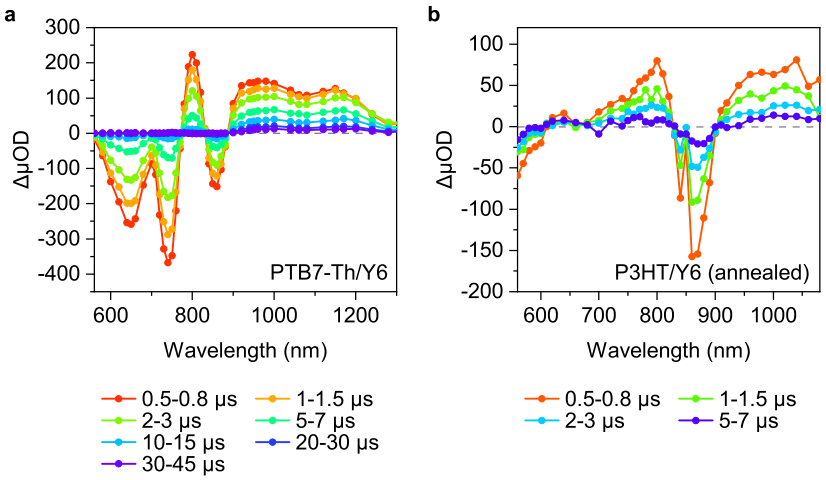

Fig. S18. TA spectra of the (**a**) PTB7-Th/Y6 and (**b**) annealed P3HT/Y6 blend films on the microsecond time scale. The excitation wavelength was 532 nm with a fluence of 0.6 and 3.0 μJ cm^{-2}, respectively.

Time evolution of the TA spectra of the PTB7-Th/Y6 blend film

The time evolution of the TA signals measured at 730 nm (GSB of PTB7-Th) and 1150 nm (hole polaron) were well fitted by the sum of an exponential function and a constant fraction (Fig. S16b). The time constants were found to be ~2.0 ps and ~2.2 ps for 730 nm and 1150 nm, respectively, indicating that Y6 excitons dissociate into charges on a time scale of ~2.0 ps. On the other hand, PIA at 780 nm increased more slowly, again as in the case of the PM6/Y6 blend. This curve was fitted by a sum of three exponential functions and a constant fraction (Fig. S16c). The average time constant was ~11.5 ps (each component is described in the figure caption). Thus, this rise is apparently slower than that of exciton dissociation, but considerably faster than the decay of hole polarons (~1.8 ns, monitored at 1150 nm). These results again confirm that the ~780 nm band emerges independently of exciton dissociation and charge recombination. Rather, it should be attributed to the charge shift from the D/A interface into the bulk of the Y6 domain, as discussed in the main text.

Excitation fluence dependence of exciton decay kinetics

Fig. S19 shows the excitation-fluence dependence of the time evolution on an early time scale monitored at 630 nm (PM6 GSB) and 830 nm (Y6 GSB). As we selectively excite Y6, only hole polarons are responsible for PM6 GSB, and hence PM6 GSB appears only when Y6 excitons dissociate into charges at the D/A interface; thereby, the rise rate of PM6 GSB is exactly the same with the decay rate of Y6 excitons. The rise kinetics of PM6 GSB as well as the decay kinetics of Y6 GSB were independent of the excitation fluence at <3.5 μJ cm^{-2}, indicating that SSA of Y6 excitons can be ignored in the blend film at low excitation fluences. On the other hand, the rise and decay kinetics become faster with increasing excitation fluence, indicating the contribution of SSA to the deactivation of Y6 singlet excitons.

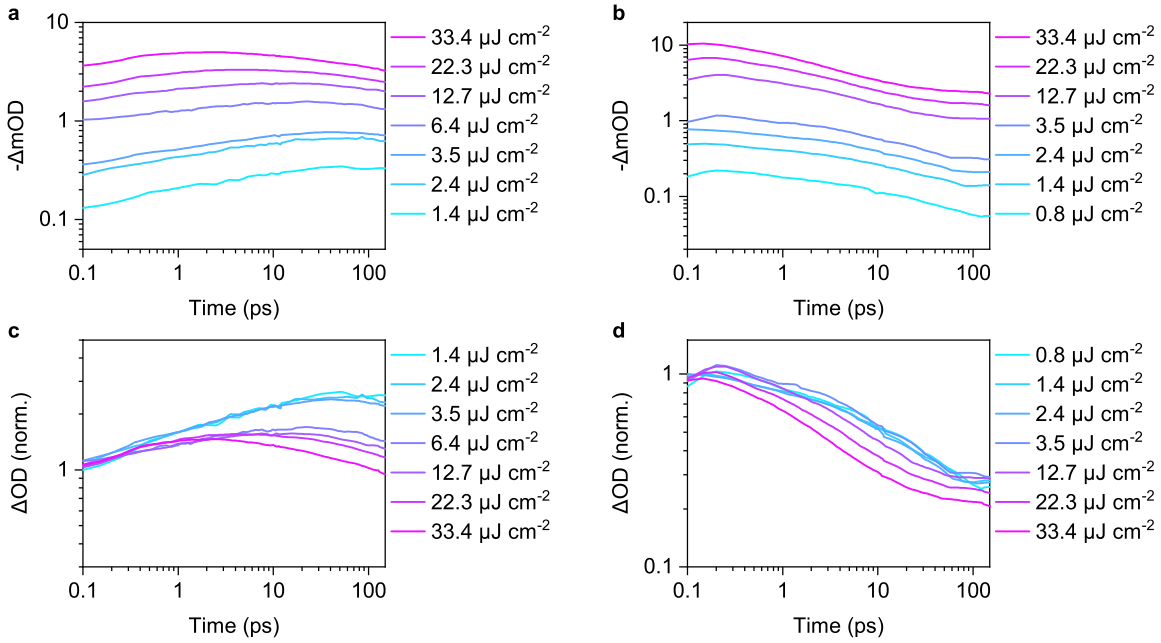

Fig. S19. **a** Rise kinetics of PM6 GSB monitored at 630 nm after photoexcitation at 800 nm. **b** Decay kinetics of Y6 GSB monitored at 830 nm after photoexcitation at 800 nm. **c**,**d** Normalized rise and decay kinetics of **a** and **b**, respectively.

Charge generation kinetics in the PM6/Y6 blend

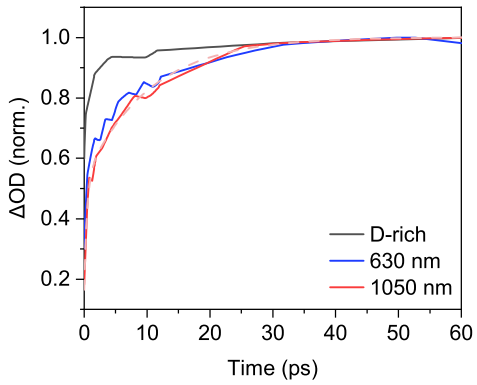

Fig. S20. Normalized time evolution of TA signals for the optimized PM6/Y6 blend film monitored at 630 (blue) and 1050 (red) nm. The excitation wavelength was 800 nm with a fluence of 1.4 μJ cm^{-2}. The rise at 1050 nm was fitted using the sum of two exponential functions with the time constants of 0.4 ps (43%) and 10.2 ps (57%) and a constant fraction (broken line). The grey line shows normalized time evolution of TA signals for the D-rich PM6/Y6 blend film monitored at 970 nm.

TA spectra of the PM6/Y6 blend film after band-edge excitation

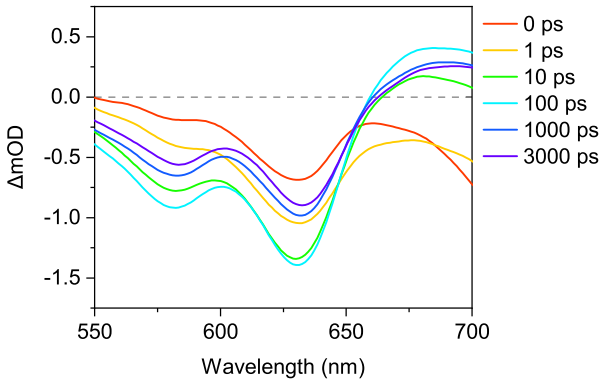

Fig. S21. TA spectra of the PM6/Y6 blend film in the visible region. The excitation wavelength was 900 nm with a fluence of 13.3 μJ cm^{-2}.

Reorganization energy

The reorganization energy was calculated by using model compounds of isolated PM6 dimer and Y6 monomer, wherein alkyl side chains were shortened to reduce the computational effort, as shown in Fig. S22. The total reorganization energy λ (Fig. S23) was calculated to be ~0.27 eV, of which ~0.19 eV was derived from PM6 and ~0.08 eV from Y6. The smaller λ of Y6 is consistent with its relatively high crystallinity.

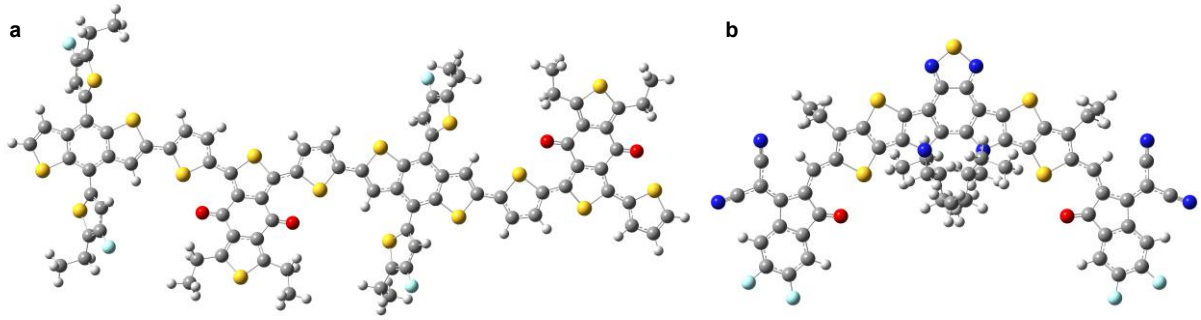

Fig. S22. Optimized structures of model compounds in the charged state obtained by the DFT calculations; **a** PM6 dimer, and **b** Y6.

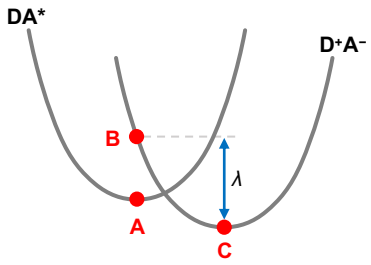

Fig. S23. Schematic defining the reorganization energy λ, which was calculated as the difference in total energies at the points **B** and **C**. The total energy at the point **B** was calculated as a sum of the total energies obtained by single point calculations of PM6 dimer and Y6 in the charged states using the geometry at the point **A**, where PM6 dimer was optimized in the ground state, whereas Y6 in the singlet excited state. The total energy at the point **C** was calculated as a sum of the total energies of the optimized PM6 dimer and Y6 in the charged states.

Late emergence of the 760 nm signal in the PM6/Y6 blend film

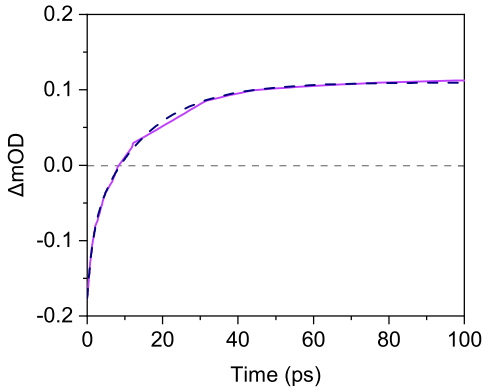

Fig. S24. Time evolution of TA signals for the optimized PM6/Y6 blend film monitored at 760 nm. The excitation wavelength was 800 nm with a fluence of 1.4 μJ cm^{-2}. The rise kinetics at 760 nm was fitted using the sum of two exponential functions with the time constants of 1.5 ps (31%) and 14.8 ps (69%) and a constant fraction (blue broken line).

Supplementary comment on the Y6 GSB peak shift

Here, we provide an additional explanation for the Y6 GSB shift. As the density of states (DOS) of organic semiconductors in the solid state is widely distributed in energy, charges generated at the D/A interface are relaxed to the lower energy sites, that is, downhill energy relaxation. We consider the absorption spectrum of the molecule occupied by the charge at each time. As the steady-state absorption spectrum of Y6 is redshifted with increasing crystallinity (Fig. S4), the absorption spectrum of the molecule occupied by the charge is redshifted during downhill relaxation. Since the GSB signal is caused by a decrease in the steady-state absorption owing to excitation of the molecule, the GSB signal reflects where the transient species resides at each time. Therefore, we conclude in the main text that the GSB redshift can be rationalized by downhill relaxation.

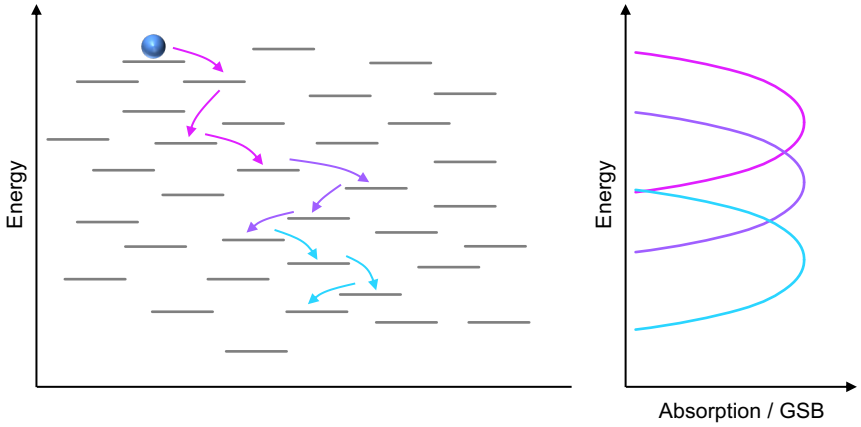

Fig. S25. Schematic showing downhill energy relaxation of charges in DOS and the corresponding absorption/GSB spectra.

Time evolution of EA

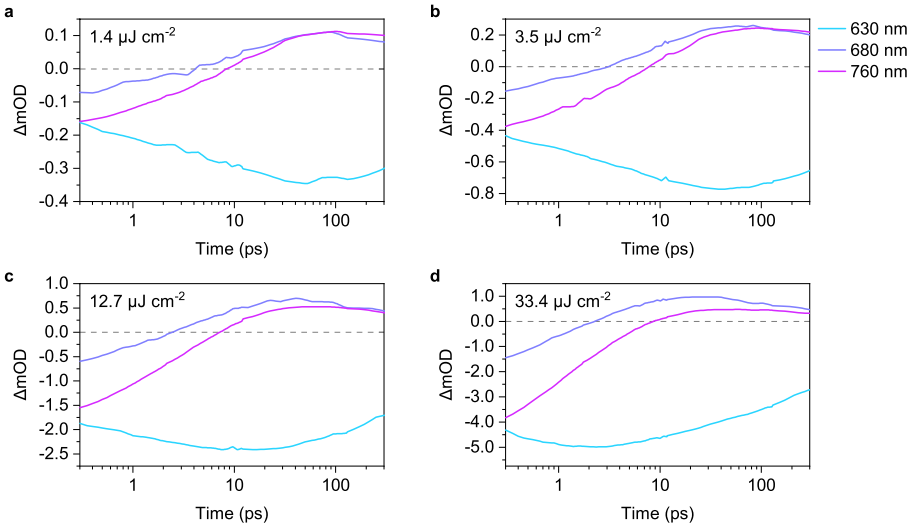

Fig. S26. Time evolutions of TA signals after photoexcitation at 800 nm with various excitation fluences.

Normalized time evolution of EA

The TA signals in Fig. S26 are normalized to clarify the differences in peak positions, as follows. First, the TA signal at 0.1 ps was subtracted from the entire signal. Then, the remaining signal was divided by its largest absolute value to provide values in the 0–1 range (Fig. S27). It should be emphasized that the above data prosessing does not change the time at which the TA signal approaches the maximum (absolute) value. In other words, the fact that the (absolute) maximum values of the EA signals were observed slightly after the hole transfer is independent of how these data are normalized.

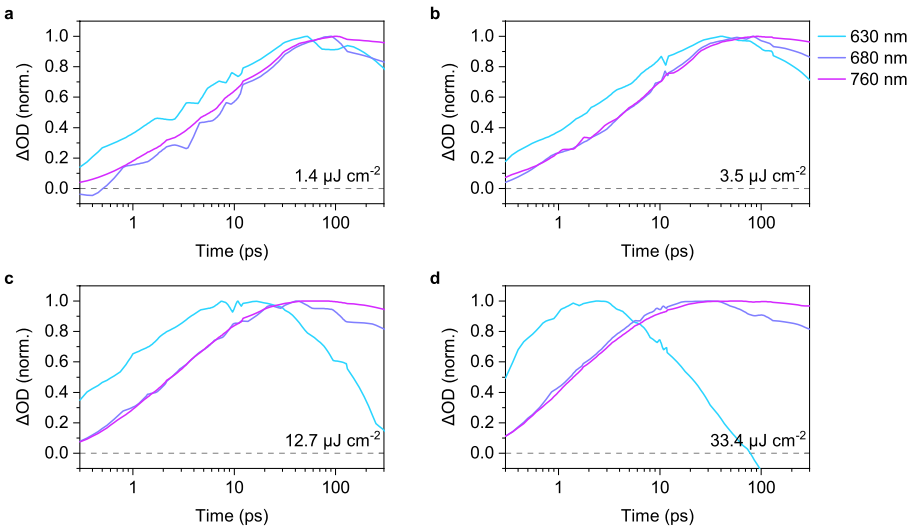

Fig. S27. Normalized time evolutions of TA signals after photoexcitation at 800 nm with various excitation fluences.

Difference in the time evolution of charge TA and EA signals

When an exciton dissociates to form an electron–hole pair at the D/A interface, the electron–hole pair generates a dipole-like local electric field. Surrounding molecules in the ground state are therefore perturbed by the local electric field, resulting in a Stark shift in the steady-state absorption spectrum. The pump-probe TA spectroscopy monitoring of the intensity difference between the transmitted probe pulse with and without pump pulse is equivalent to monitoring the intensity difference between the transmitted probe pulse with and without the local electric field. As a result, a transient EA spectrum is necessarily included in the TA spectrum.

Fig. S28 is a schematic showing the difference in the time evolution of charge TA and transient EA signals. The signal amplitude of the charge TA remains unchanged during charge dissociation process as it is a function of the charge density. In contrast, because that of the transient EA signal is a function of both the charge density and the separation distance between the electron and hole, it increases with increasing the separation distance. Therefore, the fact that the EA signals reached their maximum value slightly after the occurrence of hole transfer, as shown in Fig. 5b, indicates that long-range spatial dissociation of CT states takes place on a time scale of picoseconds.

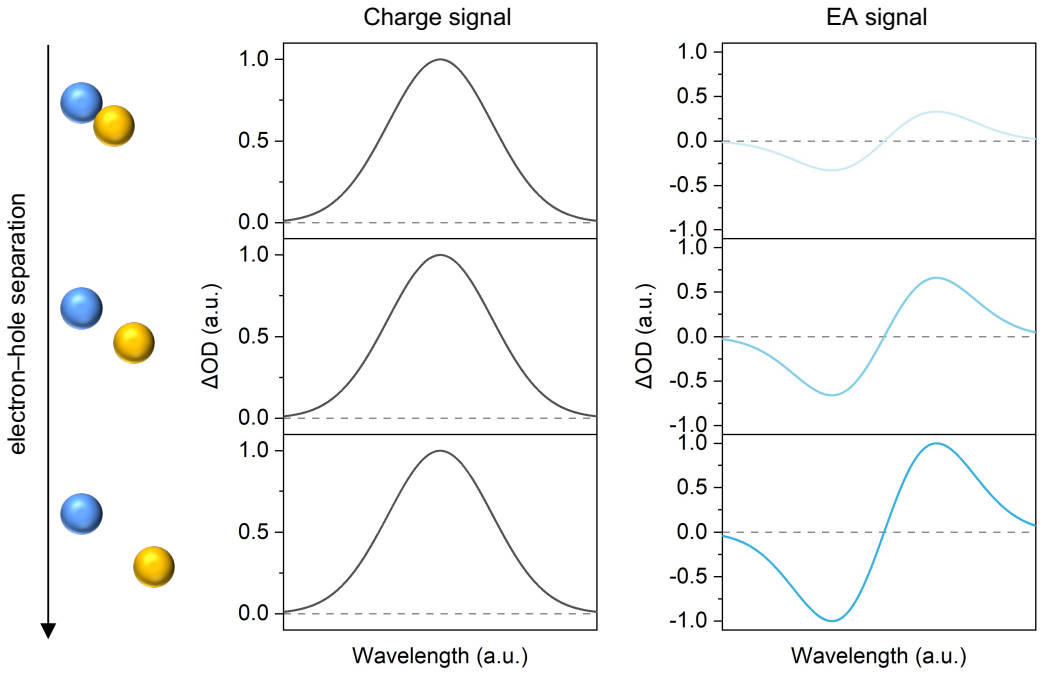

Fig. S28. Schematic showing the difference in the time evolution of charge TA and EA signals.

TA spectra of the PM6/Y6 blend film after polymer selective excitation

Fig. S29a shows the TA spectra of the PM6/Y6 blend film excited at 600 nm. The singlet excitons of PM6 observed at 1200 nm decayed very rapidly, accompanied by an increase in Y6 GSB. As shown in Fig. S29b, the time constant of the decay (rise) was found to be ~0.6 ps (~0.5 ps), indicating fast electron transfer from PM6 to Y6.

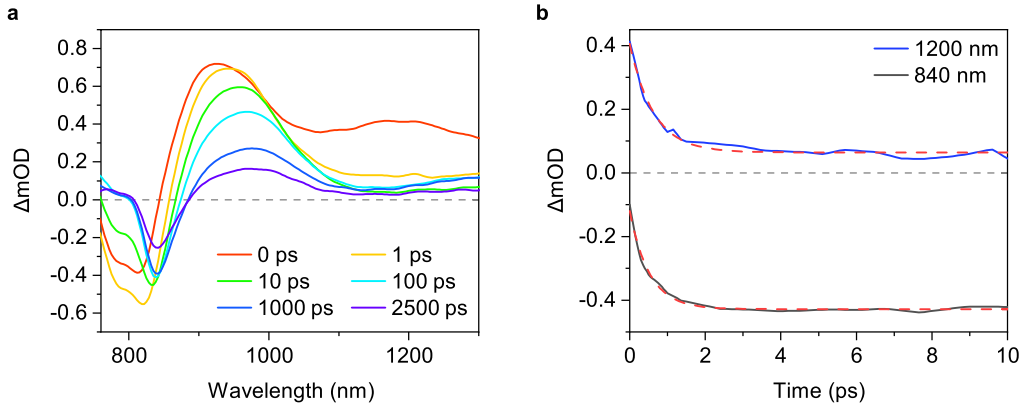

Fig. S29. **a** TA spectra of the PM6/Y6 blend film. The excitation wavelength was 600 nm with a fluence of 5.0 μJ cm^{-2}. **b** Time evolutions of PM6 singlet excitons at 1200 nm (blue) and Y6 GSB at 840 nm (black). The red broken lines are the best fits by a sum of an exponential function and a constant fraction.

Excitation fluence dependence of charge decay kinetics

Fig. S30 shows the excitation-fluence dependence of the decay kinetics of Y6 GSB monitored at 850 nm on a later time scale. GSB signals recovered faster with increasing excitation fluence even under low excitation fluences, suggesting that the FC generation is efficient and hence, bimolecular charge recombination is the dominant decay channel for the PM6/Y6 blend film.

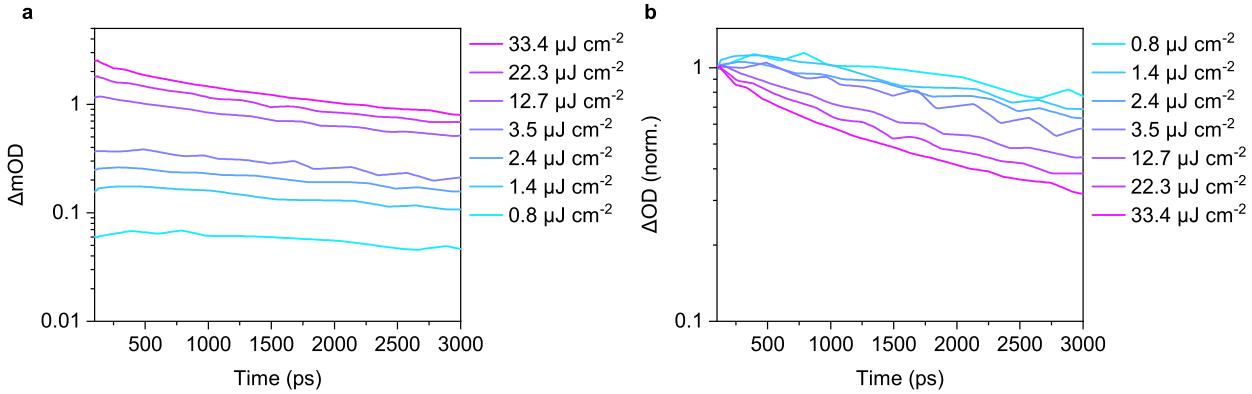

Fig. S30. **a** Decay kinetics of Y6 GSB monitored at 850 nm after photoexcitation at 800 nm. **b** Normalized kinetics of **a**.

Temperature dependence of the PM6/Y6 blend

The TA signals at 780 nm increased with decreasing temperature because the GSB band red-shifted with decreasing temperature (Fig. S32a), thereby mitigating the spectral overlap between the positive PIA and the GSB. It should be noted that this complicated temperature dependence at 780 nm does not affect our conclusion.

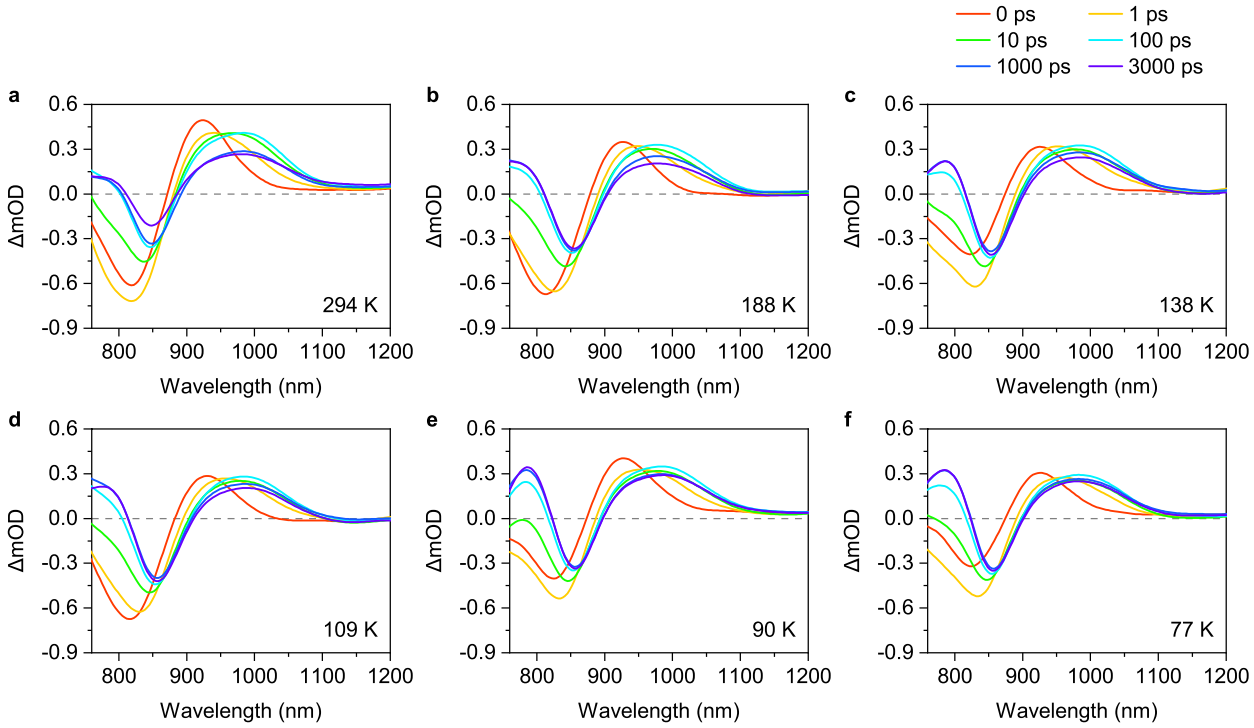

Fig. S31. TA spectra of the PM6/Y6 blend film measured at various temperatures.

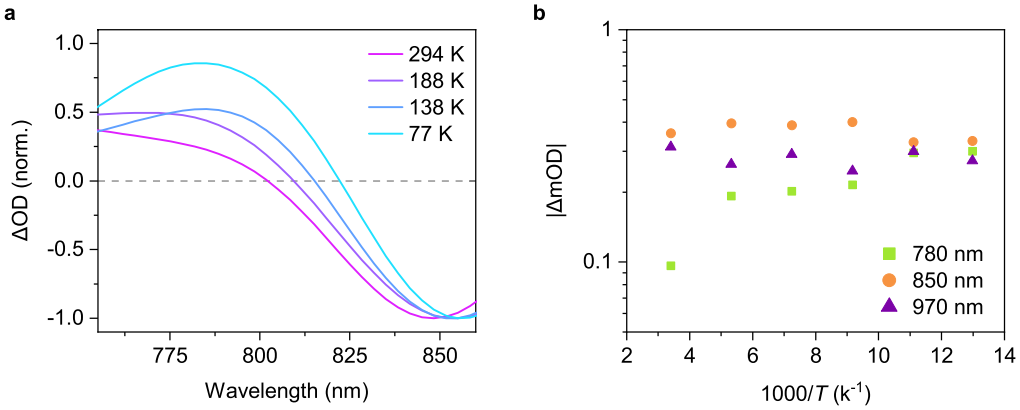

Fig. S32. **a** Normalized TA spectra of the PM6/Y6 blend film at 500 ps after photoexcitation measured at various temperatures. **b** Arrhenius plot for the TA amplitude.

Fig. S33 shows the Arrhenius plot for the inverse of the rise time constant k_{rise} monitored at 780 nm (same as Fig. 7c). The red line shows the best fit curve with the following Arrhenius equation using four data points on the left side

$$k_{\mathrm{rise}} = A\exp\left(-\frac{E_{\mathrm{a}}}{k_{\mathrm{B}}T}\right) \tag{S2}$$

where E_a is the activation energy. E_a was determined to be ~9.4 meV, which is the upper limit of the estimation. On the other hand, we obtained the green curve with E_a of ~4.0 meV when all data points were used for the fitting.

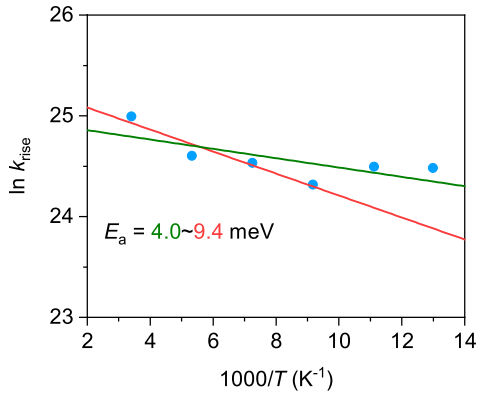

Fig. S33. Arrhenius plot for the inverse of the rise time constant k_{rise} monitored at 780 nm. The solid lines represent the best fit curves with Equation S2.

Triplet generation via bimolecular charge recombination

Fig. S34a shows the TA spectra of the PM6/Y6 blend film at a high excitation fluence. A long-lived PIA is pronounced at ~1400 nm at later times (Fig. S34b), which is attributable to Y6 triplet excitons generated through bimolecular charge recombination.[S6,S7]

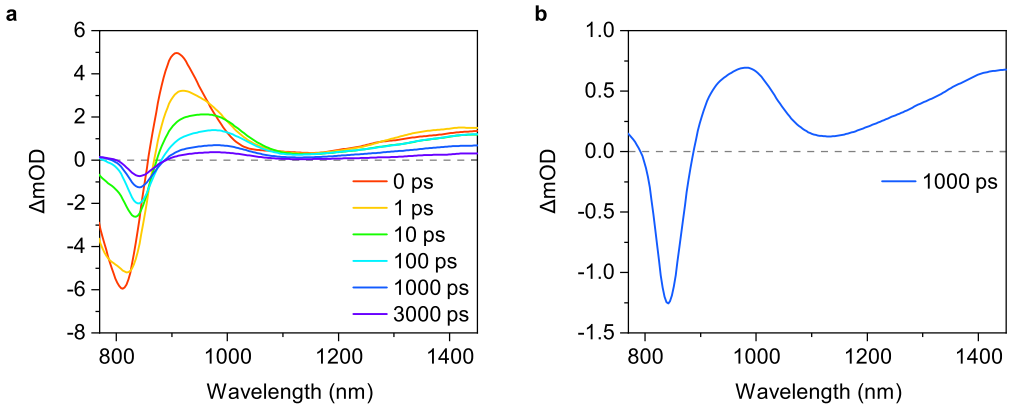

Fig. S34. **a** TA spectra of the PM6/Y6 blend film. The excitation wavelength was 800 nm with a fluence of 22.3 μJ cm^{-2}. **b** Enlarged TA spectra at 1000 ps.

TA data processing via total variation regularization

Herein, we introduce a new denoising method for time-resolved spectroscopy based on the total variation (TV) regularization. The original TV regularization method was introduced in the context of digital image restoration under Gaussian noise[S19] and has now evolved into a more general technique for solving inverse problems.

In this method, we assume that the degradation of the observed TA data $\mathbf{v} \in \mathbb{R}^{m\times n}$ can be modeled as

$$\mathbf{v} = \bar{\mathbf{u}} + \mathbf{n} \tag{S3}$$

where $\bar{\mathbf{u}} \in \mathbb{R}^{m\times n}$ is an unknown original noise-free signal, and $\mathbf{n} \in \mathbb{R}^{m\times n}$ is an additive noise. Owing to the continuity of both the absorption spectra of organic molecules and their decay kinetics, we can assume that $\bar{\mathbf{u}}$ is piecewise smooth, i.e. the second derivative of $\bar{\mathbf{u}}$ is sparse.

By letting $\mathbf{D}_{\boldsymbol{x}}, \mathbf{D}_{\boldsymbol{y}} \in \mathbb{R}^{m\times m}$ be the vertical and horizontal discrete gradient operators, respectively, with the Newmann boundary, the TV of the second order for each direction of the TA data matrix is given as

$$\mathrm{TV}_{x,y}(\boldsymbol{u}) := \mathbf{D}_{x,y}^{\mathbf{2}}\boldsymbol{u} \tag{S4}$$

For example

$$\mathbf{D}_x := \begin{pmatrix} -1 & 1 & 0 & 0 & \cdots & 0 \\ 0 & -1 & 1 & 0 & \cdots & 0 \\ \vdots & & \ddots & \ddots & & \vdots \\ 0 & \cdots & 0 & -1 & 1 & 0 \\ 0 & \cdots & 0 & 0 & -1 & 1 \\ 0 & \cdots & 0 & 0 & 0 & 0 \end{pmatrix} \tag{S5}$$

Therefore, to obtain $\bar{\mathbf{u}}$, the following convex optimization problem should be solved:

$$\min_{\mathbf{u}\in\mathbb{R}^{m\times n}} \lambda_1 \|\mathrm{TV}_x(\boldsymbol{u})\|_p + \lambda_2 \left\|\mathrm{TV}_y(\boldsymbol{u})\right\|_p \quad \text{s.t.} \quad \mathbf{u} \in B_\varepsilon \tag{S6}$$

where

$$B_\varepsilon := \|\mathbf{v} - \mathbf{u}\|_2 \le \varepsilon \tag{S7}$$

The set B_ε is a **v**-centred l_2-norm ball with a radius ε, which serves as a fidelity constraint with respect to the observation **v**. Prefactors λ_1 and λ_2 determine the balance between the vertical and horizontal TV terms, respectively, and $\| * \|_p$ (p = 1 or 2) stands for the l_1- and l_2-norm, i.e. the sum of absolute values of all the entries of (*) and the Euclidean norm, respectively.

To solve Equation S6, we used a primal-dual splitting method,[S20,S21] which can solve optimization problems of the form:

$$\underset{\mathbf{x}\in\mathbb{R}^{m\times n}}{\operatorname{argmin}} f(\mathbf{x}) + \mathrm{g}(\mathbf{x}) + h(\mathbf{L}\mathbf{x}) \tag{S8}$$

where f is a differentiable convex function with the β-Lipschitzian gradient ∇f for some $\beta > 0$, g and h are proximable functions, and **L** is a matrix. The algorithm is given by

$$\mathbf{x}^{(n+1)} = \mathrm{prox}_{\gamma_1 g}\left[\mathbf{x}^{(n)} - \gamma_1\left(\nabla f\left(\mathbf{x}^{(n)}\right) + \mathbf{L}^*\right)\right] \quad \text{(S9)}$$

$$\mathbf{y}^{(n+1)} = \mathrm{prox}_{\gamma_2 h^*}\left[\mathbf{y}^{(n)} + \gamma_2 \mathbf{L}\left(2\mathbf{x}^{(n+1)} - \mathbf{x}^{(n)}\right)\right] \quad \text{(S10)}$$

where prox denotes the proximity operator, h^* is the Fenchel-Rockafellar conjugate function[S22] of h, and $\mathbf{L}^*$ is the adjoint operator of $\mathbf{L}$. In addition, γ_1 and γ_2 (γ_1, $\gamma_2 > 0$) are the step sizes that satisfy $\gamma_1^{-1} - \gamma_2\lambda_1(\mathbf{L}^*\mathbf{L}) \geqq \beta/2$, where $\lambda_1(*)$ stands for the maximum eigenvalue of *. Under some mild conditions of g, h, and $\mathbf{L}$, the sequence converges to a solution for Equation S8.

Here, we demonstrate TV denoising for TA spectroscopy. Fig. S35a shows the TA data of the PM6/Y6 blend film measured under a high excitation fluence of 50 μJ cm^{-2}. Owing to the high excitation fluence, the SNR of the data was reasonably high without any denoising methods. Therefore, we used these data as a "*known*" $\bar{\mathbf{u}}$. Then, we added Gaussian noise to artificially degrade the data (Fig. S35b).

Before applying TV denoising, we performed a normal moving average method for the degraded data (Figs. S35c,d). Denoised data labeled "movave 1" and "movave 2" represent the data obtained by the moving average method, wherein the i,j-th data are replaced by an average over between the $i\pm2,j\pm2$-th, and $i\pm5,j\pm5$-th data, respectively (i.e. the window size of "movave 1" and "movave 2" are 5 and 11, respectively). The residue of the Gaussian noise was observed when the window size of the moving average was 5 ("movave 1", Figs. S35c and S37a, blue line). On the other hand, although the residue was mitigated when the window size was 11 ("movave 2", Figs. S35d and S37a, green line), the edge feature around the time origin is lost for "movave 2" (Fig. S37c, green line). For a more quantitative discussion, we evaluated the root mean squared error (RMSE) between the original and noisy/denoised data. As shown in Fig. S36a, the RMSE of the "movave 1" and "movave 2" data were ~4.9 and ~8.3 times smaller than that of the artificially degraded data, respectively. We also evaluated the slope at the time origin and compared to that of the original data. The relative slope obtained by a linear fit to the onset around the time origin decreased to ~0.64 and ~0.42, respectively, for the "movave 1" and "movave 2" data, meaning that the apparent time resolution of the TA data degrades with increasing the window size. These results indicate that it is difficult to simultaneously remove noise and retain edges using the moving average method.

Figs. S35e–g show data denoised using the TV regularization method with different p values (details can be found in the caption of Fig. S35). We found that all TV data with different p values exhibited a lower RMSE and a better apparent time resolution than those obtained using the moving average method (Fig. S36). We obtained the best solution by the TV regularization method with $p = 2$ (l_2-norm) for the vertical (spectrum) direction and $p = 1$ (l_1-norm) for the horizontal (kinetics) direction, as shown in Figs. S36 and S37. The RMSE

is ~9.9 times smaller than that of the artificially degraded data, although the relative slope at the onset remained as large as ~0.88. Notably, the TV regularization method demonstrated here is also advantageous for maintaining the wavelength resolution for the same reasons. We could obtain denoised TA kinetics data if the TA data were averaged over the vertical direction. However, this is equivalent to degrading the apparent wavelength resolution of the TA data, which is undesirable when the TA data consist of a superposition of various transient species. In contrast, the TV regularization method maintain the apparent wavelength resolution.

It should be emphasized that this method is effective for any kind of time-resolved spectroscopic techniques such as time-resolved PL, THz, microwave conductivity measurements. In summary, TV regularization method demonstrated here is a highly effective denoising method for time-resolved spectroscopic techniques.

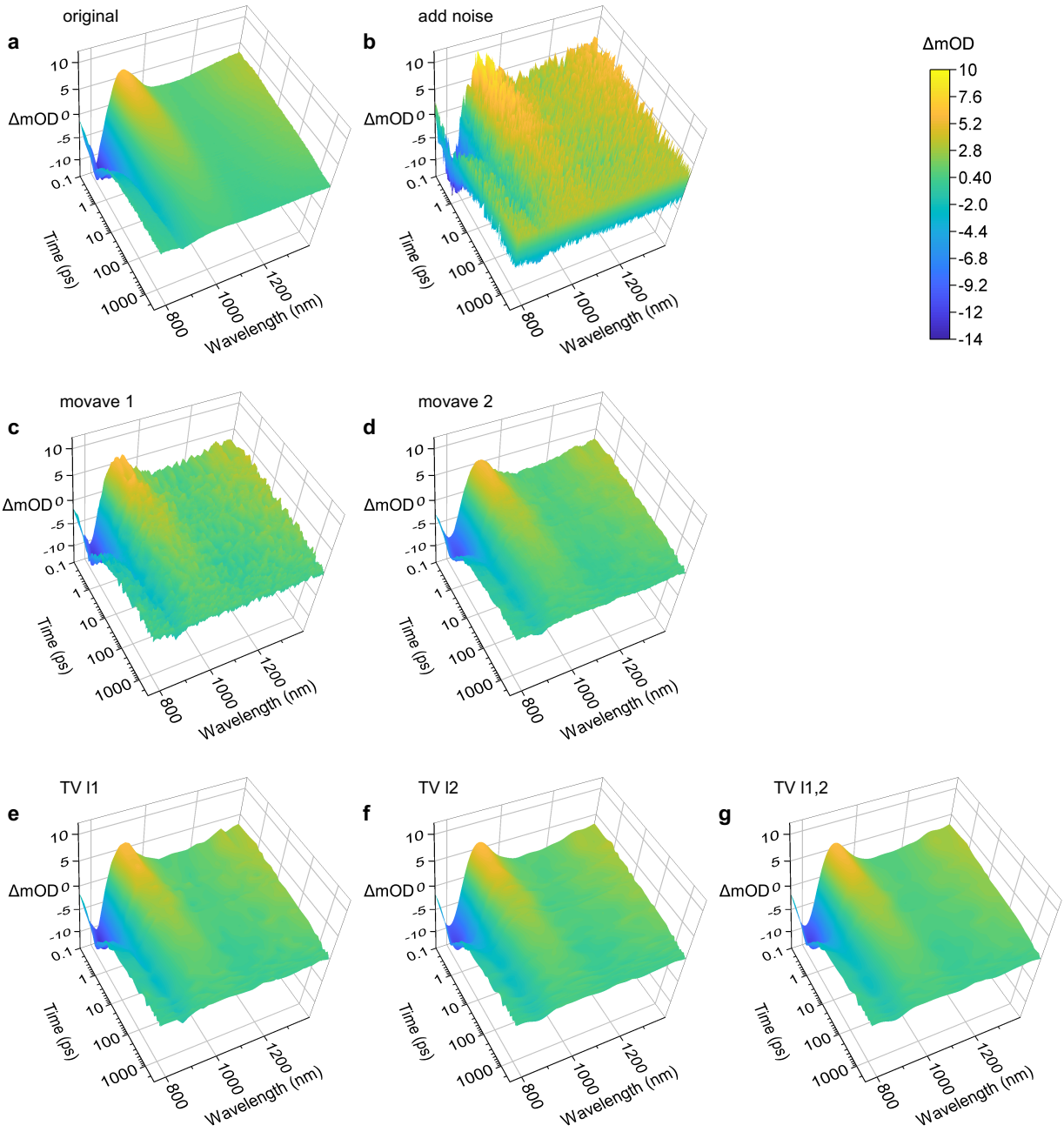

Fig. S35. Surface plot of various datasets. Original: original TA data; add noise: artificially degraded data by adding a Gaussian noise; movave 1,2: denoised data by the moving average method with different window sizes (window size: "movave 1" = 5, "movave 2" = 11); TV l1 and TV l2: data denoised using by the TV regularization method with p = 1 (l_1-norm) and 2 (l_2-norm), respectively; TV l1,2: data denoised using the TV regularization method with p = 2 (l_2-norm) for the vertical direction and p = 1 (l_1-norm) for the horizontal direction.

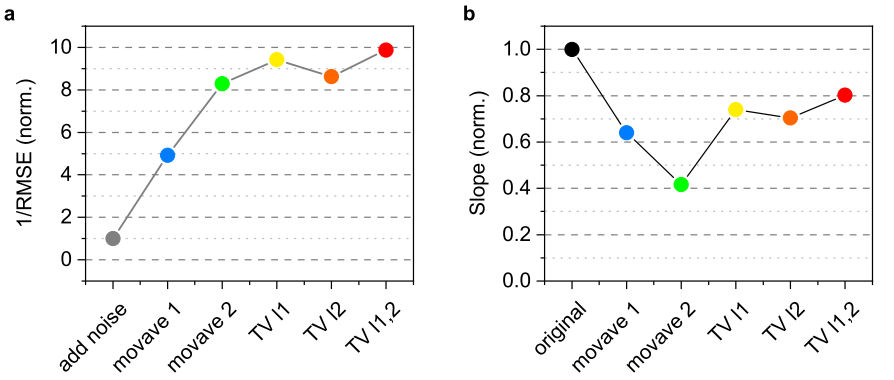

Fig. S36. **a** Inverse of the normalized RMSE. **b** Normalized slope of the onset. Slope for "add noise" could not be determined due to the serious noise.

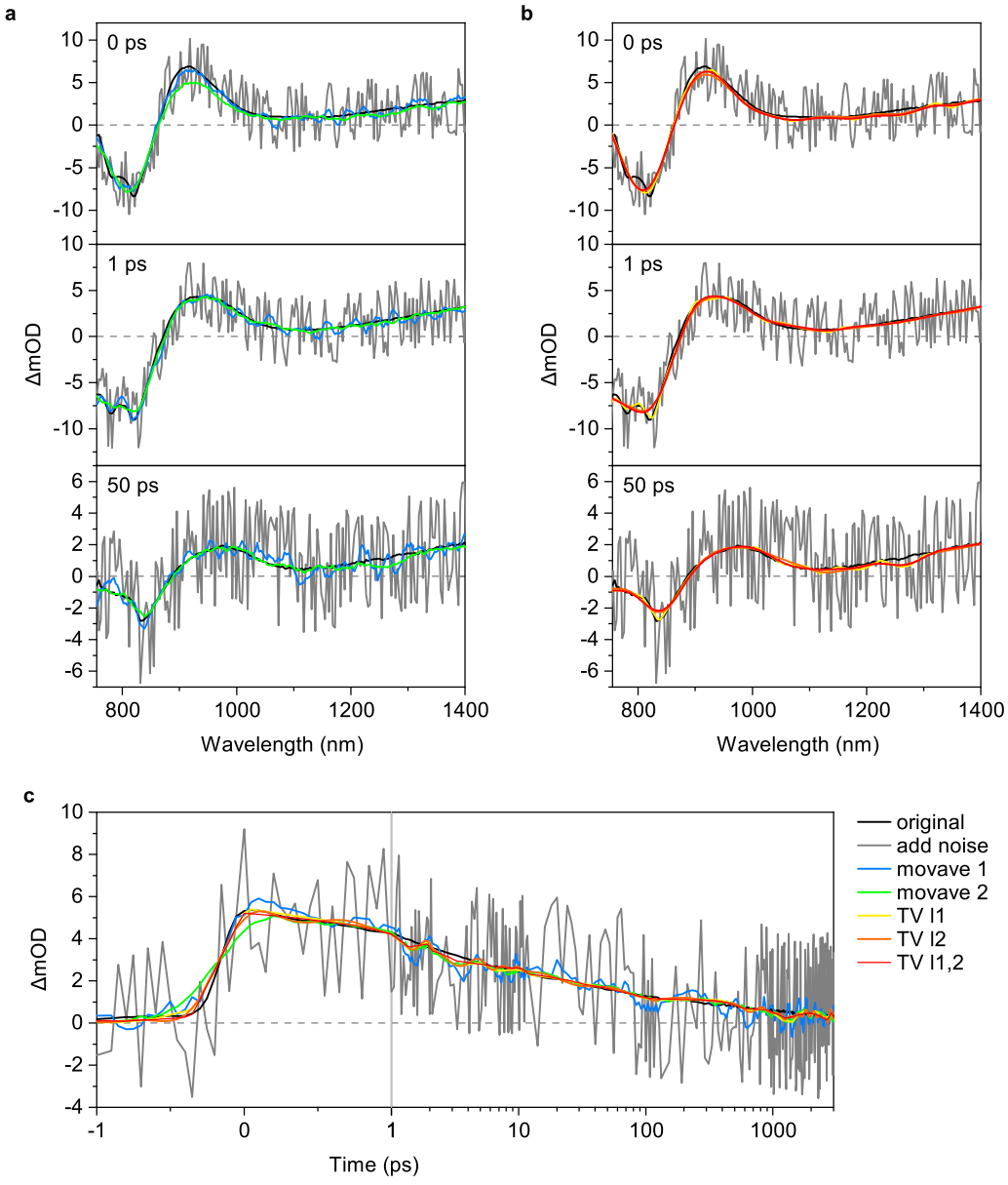

Fig. S37. **a** TA spectra denoised by the moving average method. **b** TA spectra denoised by the TV regularization method. **c** Time profiles obtained by various denoising methods.

References

S1. H. Ohkita, Y. Tamai, H. Benten, S. Ito, *IEEE J. Sel. Top. Quantum Electron.* 2016**, 22**, 100-111.

S2. M. J. Frisch, G. W. Trucks, H. B. Schlegel, G. E. Scuseria, M. A. Robb, J. R. Cheeseman, G. Scalmani, V. Barone, G. A. Petersson, H. Nakatsuji, X. Li, M. Caricato, A. V. Marenich, J. Bloino, B. G. Janesko, R. Gomperts, B. Mennucci, H. P. Hratchian, J. V. Ortiz, A. F. Izmaylov, J. L. Sonnenberg, Williams, F. Ding, F. Lipparini, F. Egidi, J. Goings, B. Peng, A. Petrone, T. Henderson, D. Ranasinghe, V. G. Zakrzewski, J. Gao, N. Rega, G. Zheng, W. Liang, M. Hada, M. Ehara, K. Toyota, R. Fukuda, J. Hasegawa, M. Ishida, T. Nakajima, Y. Honda, O. Kitao, H. Nakai, T. Vreve, K. Throssell, J. A. Montgomery Jr., J. E. Peralta, F. Ogliaro, M. J. Bearpark, J. J. Heyd, E. N. Brothers, K. N. Kudin, V. N. Staroverov, T. A. Keith, R. Kobayashi, J. Normand, K. Raghavachari, A. P. Rendell, J. C. Burant, S. S. Iyengar, J. Tomasi, M. Cossi, J. M. Millam, M. Klene, C. Adamo, R. Cammi, J. W. Ochterski, R. L. Martin, K. Morokuma, O. Farkas, J. B. Foresman and D. J. Fox, *Gaussian 16 Rev. A.01*, Wallingford, CT, 2016.

S3. K. Jiang, Q. Wei, J. Y. L. Lai, Z. Peng, H. K. Kim, J. Yuan, L. Ye, H. Ade, Y. Zou and H. Yan, *Joule*, 2019, **3**, 3020-3033.

S4. A. Karki, J. Vollbrecht, A. J. Gillett, S. S. Xiao, Y. Yang, Z. Peng, N. Schopp, A. L. Dixon, S. Yoon, M. Schrock, H. Ade, G. N. M. Reddy, R. H. Friend and T.-Q. Nguyen, *Energy Environ. Sci.*, 2020, **13**, 3679-3692.

S5. L. Xu, W. Tao, H. Liu, J. Ning, M. Huang, B. Zhao, X. Lu and S. Tan, *J. Mater. Chem. A*, 2021, **9**, 11734-11740.

S6. S. Natsuda, Y. Sakamoto, T. Takeyama, R. Shirouchi, T. Saito, Y. Tamai, H. Ohkita, *J. Chem. Phys. C*, 2021, **125**, 20806-20813.

S7. A. J. Gillett, A. Privitera, R. Dilmurat, A. Karki, D. Qian, A. Pershin, G. Londi, W. K. Myers, J. Lee, J. Yuan, S.-J. Ko, M. K. Riede, F. Gao, G. C. Bazan, A. Rao, T.-Q. Nguyen, D. Beljonne, R. H. Friend, *Nature*, 2021, **597**, 666-671.

S8. L. Perdigón-Toro, L. Q. Phuong, S. Zeiske, K. Vandewal, A. Armin, S. Shoaee, D. Neher, *ACS Energy Lett.*, 2021, **6**, 557-564.

S9. K. Vandewal, K. Tvingstedt, A. Gadisa, O. Inganäs and J. V. Manca, *Phys. Rev. B*, 2010, **81**, 125204.

S10. K. Vandewal, K. Tvingstedt, J. V. Manca and O. Inganäs, *IEEE J. Sel. Top. Quantum Electron.*, 2010, **16**, 1676-1684.

S11. P. Wan, X. Chen, Q. Liu, S. Mahadevan, M. Guo, J. Qiu, X. Sun, S.-W. Tsang, M. Zhang, Y. Li, S. Chen, *J. Phys. Chem. Lett.*, 2021, **12**, 10595-10602.

S12. J. Yuan, Y. Q. Zhang, L. Y. Zhou, G. C. Zhang, H. L. Yip, T. K. Lau, X. H. Lu, C. Zhu, H. J. Peng, P. A. Johnson, M. Leclerc, Y. Cao, J. Ulanski, Y. F. Li and Y. P. Zou, *Joule*, 2019, **3**, 1140-1151.

S13. C. M. Cardona, W. Li, A. E. Kaifer, D. Stockdale, G. C. Bazan, *Adv. Mater.*, 2011, **23**, 2367-2371.

S14. S. Karuthedath, J. Gorenflot, Y. Firdaus, N. Chaturvedi, C. S. P. De Castro, G. T. Harrison, J. I. Khan, A. Markina, A. H. Balawi, T. A. D. Peña, W. Liu, R.-Z. Liang, A. Sharma, S. H. K. Paleti, W. Zhang, Y. Lin, E. Alarousu, D. H. Anjum, P. M. Beaujuge, S. De Wolf, I. McCulloch, T. D. Anthopoulos, D. Baran, D. Andrienko and F. Laquai, *Nat. Mater.*, 2021, **20**, 378-384.

S15. T. Umeyama, K. Igarashi, D. Sasada, Y. Tamai, K. Ishida, T. Koganezawa, S. Ohtani, K. Tanaka, H. Ohkita and H. Imahori, *Chem. Sci.*, 2020, **11**, 3250-3257.

S16. T. Umeyama, K. Igarashi, Y. Tamai, T. Wada, T. Takeyama, D. Sasada, K. Ishida, T. Koganezawa, S. Ohtani, K. Tanaka, H. Ohkita and H. Imahori, *Sustain. Energy Fuels*, 2021, **5**, 2028-2035.

S17. Y. Tamai, Y. Fan, V. O. Kim, K. Ziabrev, A. Rao, S. Barlow, S. R. Marder, R. H. Friend and S. M. Menke, *ACS Nano*, 2017, **11**, 12473-12481.

S18. J. Guo, H. Ohkita, S. Yokoya, H. Benten and S. Ito, *J. Am. Chem. Soc.*, 2010, **132**, 9631-9637.

S19. L. I. Rudin, S. Osher and E. Fatemi, *Physica D*, 1992, **60**, 259.

S20. L. Condat, *J. Optim. Theory Appl.*, 2013, **158**, 460-479.

S21. B. C. Vũ, *Adv. Comput. Math.*, 2013, **38**, 667-681.

S22. S. K. Narang and A. Ortega, *IEEE Trans. Signal Process.*, 2013, **61**, 4673-4685.